Joule, Volume *6*

Supplemental information

Photoprotection in metal halide perovskites

by ionic defect formation

Nga Phung, Alessandro Mattoni, Joel A. Smith, Dieter Skroblin, Hans Köbler, Leo Choubrac, Joachim Breternitz, Jinzhao Li, Thomas Unold, Susan Schorr, Christian Gollwitzer, Ivan G. Scheblykin, Eva L. Unger, Michael Saliba, Simone Meloni, Antonio Abate, and Aboma Merdasa

Supplemental Experimental Procedures

Note S1: Photoluminescence microscopy

In this study, we focused light from a diode laser (λ_{ex} = 450 nm or photon energy of 2.75 eV) into a spot having a Gaussian-like profile with a FWHM of 6 μm (**Figure S1a**). With a maximum output power of 2.48 mW from the laser reaching the sample, we obtained an average excitation power density (EPD) of 2.55 kW/cm^2 at FWHM (~26,000 Sun). Resolving the excitation profile in space, the maximum EPD at the centre of the excitation spot is nearly 4 kW/cm^2. Assuming the spot is radially symmetric, we limit our investigations to one spatial dimension as indicated by the red-shaded plane (**Figure S1a**). Reducing the spatial dimension to only one allows us to extract spectra at every point along the resulting line drawn in red in **Figure S1a**. This approach provides an opportunity to probe the power dependence on PL spectral features at a single instant by simply comparing spectra acquired at different positions along the excitation profile (depicted as a red line in **Figure S1a**). All spectra generated at the line profile are then recorded with a time-resolution of 100 ms, which further allows us to track how the spectra evolves in space.

Prior to measuring the spatially resolved spectra, we recorded a sequence of PL images in which we excited a thin $MAPbI_3$ film with the highest EPD. We observe changes in the relative PL quantum yield evolving in space on a timescale of seconds shown in the sequence of selected PL images in Error! Reference source not found.**b**. Initially (t = 0 s), the spatial distribution of the PL intensity follows that of the laser excitation profile shown in Error! Reference source not found.**a**. As can be seen in **Figure S1b** and **Figure S1e**, within a few seconds (t = 3 s), the PL intensity radically drops in the centre of the excitation spot where the EPD is highest, which yields a ring-shaped distribution of PL emission. Thereafter, PL is slightly restored in the centre (t = 10 s), after which the emissive region again spreads away from the centre (t = 15 s). This trend is not expected considering the illumination *intensity* profile remains constant in time, however, one must consider that the charge carrier density might change over time due to change in material's bandgap. We verified that the same trend was observed in repeated measurements, and concluded that it reflected a photo-induced modification of a material property, rather than a measurement artefact. Spatial redistribution of PL on slow time-scales falls in line with previous reports for similar perovskite compounds where it has been attributed to migrating/accumulating ionic species.[1–3] Similar features are apparent in studies using bias poling, which correlate the ionic defect migration to a spatially changing PL intensity,[4,5] although the non-linear behaviour here suggests more than one simultaneous photo-induced process.

In addition to the PL intensity changes, we also observe changes in peak position, quantified by ΔE_p, - the difference between low intensity PL peak position and high intensity PL peak position measurement, presented in **Figure S1d**. We notice that although at 2.5 kW/cm^2, the PL intensity shows dynamic evolution similar to the highest EPD at 3.75 kW/cm^2, whereas the PL peak shift is static (comparing green and black traces in **Figure S1e** and **Figure S1f**). We differentiate this dynamic behaviour of ΔE_p from the stable blue-shifted emission observed at lower EPDs, which we attribute to lattice expansion as the shift is linearly proportional to the EPD. This can explain the distinct features shown in **Figure S1f**, where the centre of the excitation (at EPD of 3.75 kW/cm^2) shows a complex evolution of PL peak due to ionic defect formation and possibly migration. On the other hand, the static ΔE_p trends induced by lower EPDs indicate the variation in bandgap due to thermally induced lattice expansion caused by temperature gradient, which further supports the notion that light injects heat in the lattice. This also implies a fairly constant temperature distribution immediately after the light is on (within 100 ms of measurement time resolution), hence, corroborates the time scale required for the sample to cool down in the simple heat model calculation in the next section. Therefore, the PL peak shift the centre of the excitation strongly indicates light-induced ionic defects in this case rather than purely thermal lattice expansion effect.

Prolonged measurements indicating no degradation to PbI_2

In **Figure S2** we show PL spectra heat maps with two fluxes (37500 Sun and 1870 Sun) for extended periods of time. The PL shifts shown in more detail in **Figure S1f** can be seen in **Figure S2a**, although this is followed by stabilization toward lower energies within 20 seconds of exposure. Although the PL dynamics with the minor red/blue PL shifts is likely representative of a more complex underlying dynamics including emission from a distorted lattice causing a widened bandgap combined with emission via shallow sub-gap states, we here instead emphasize here that the emission is still indicative of a perovskite lattice and not PbI_2 (no emission is observed at the dashed line where PL from PbI_2 should be expected. While there certainly could be some PbI_2 present that simply does not appear in the PL since emission occurs from the lowest accessible state ($MAPbI_3$), we can at least rule out that there exists no larger PbI_2 domains of significant size that are on the scale of the excitation profile, since we should expect at least some PbI_2 emission considering the comparatively large excitation profile of 6 um when compared to the resolving power in the detection of approximately 375 nm (NA = 0.6). Thus we conclude that the illuminated film is not degraded. Although the flux isn't at a maximum, **Figure S2b** demonstrates that this stability can be observed up to tens of minutes at a flux that is still orders of magnitude higher than standard operational conditions.

Note S2: Heat diffusion model

Charge carrier thermalisation, *i.e.*, the release of the excess energy of carriers exceeding the band gap as thermal energy to the atoms of the crystal, can heat up the material and cause bandgap shifts by lattice expansion. However, in the present case our PL experiments provide evidence that this is not the only process induced by light carriers thermalisation. In fact, in the main text we show that the effect of the release of this excess thermal energy is long lasting, well above the time it takes for a hot $MAPbI_3$ film to return to room temperature, as we show in detail in the following.

In a report by Foley *et al.*, similar bandgap shifts are observed in $MAPbI_3$ thin films when heated from 300 K to 385 K,[6] which can be explained with the unusual antibonding nature of the valence band frontier orbitals.[7] Moreover, it has been reported that 128 Sun (*i.e.* 0.0128 kW/cm^2, AM 1.5G solar spectrum) can raise temperature of a perovskite solar cells of similar composition by several tens of K.[8] However, despite irradiating the film at 3.75 kW/cm^2 (hundreds times higher), the perovskite film in this study shows no sign of melting and remains essentially intact, which we can establish by SEM images of an irradiated spot (**Figure S3a**). Instead, we measure a marginally shifting perovskite-like emission with a peak somewhere between 1.61-1.63 eV throughout the extent of our 15s measurement, which, considering the results reported in Ref.[6], suggests a maximum temperature of ~375 K. We have confirmed this hypothesis performing, for the first time, direct temperature measurements in the irradiated spot (**Figure 1** in the main text), revealing that it never exceeds 340K even with λ_{ex} = 473 nm photons.

In the main text, we propose that this low temperature is made possible due to a self-regulation mechanism of halide perovskite, that absorbs excess thermal energy by creating Frenkel pairs. To experimentally separate lattice expansion and ionic defect formation as the cause for a blue-shift, we rely on the fact that trend of the PL shifts at the highest EPD (black trace in **Figure S1f**) is reproducible. If a thermally driven process is present and gives rise to a blue-shifting PL peak, this should reverse once the film cools. A simple model of the heat diffusion in the film upon laser exposure, discussed in detail below, estimates that an extreme equilibrium temperature of 500 K will cool to room temperature well within one second once the heat supplying source (laser) is removed. Assuming a similar rate of band gap increase with temperature suggests that the temperature of our film when exposed to light at a flux of nearly 26,000 Sun is only ~375 K (based on excitation power density at 2.55 kW/cm^2 at FWHM), which is incompatible with the energy density injected into the sample by the exciting source (see below).

To address the questions above, we computed the temperature profile in the film in our experimental setup determined by solving the transient (time dependent) heat transfer equation

$$\rho C \frac{\partial T(\vec{r},t)}{\partial t} - \nabla[k \nabla T(\vec{r},t)] = q(\vec{r}),$$

where ρ, C, and k are the density, specific heat and thermal conductivity of the material value taken from Heiderhoff *et al.,*[9] q is the energy density injected by the exciting source; here we considered only the thermalisation energy, *i.e.* the excess energy carried about by the photon with respect to the band gap. $q(\vec{r})$ depends on the position as i) the excitation beam has a Gaussian profile, $I(\vec{r}) = I_0 \exp\{-[(x-x_0)^2 + (y-y_0)^2]/2\sigma^2\}$ with σ width of the beam, and photons absorption follows an exponential law, with residual photons, hence thermalization heat, following the law $q(\vec{r}) = q(x,y,z_0)\exp\{-(z_0 - z)/\lambda\}$, where $\lambda = 0.1\ mm$ is the intensity decay length of MAPbI$_3$ film due to its high absorption coefficient.[10] Any additional contribution arising from non-radiative recombination, which would further increase the heat injected into the system, has been neglected. Similarly, we did not take into account the possible radiative recombination before thermalisation, which would reduce the heat into the system: PL experiments have shown only emission arising from the recombination of cold carriers.

In **Figure S3b**, we report the colour map of the temperature $T(\vec{r},t)$ for a film subjected to an excitation beam at λ_{ex} = 450 nm (2.75 eV) after 10 s of illumination, when temperature has reached stationarity. The temperature range goes from room temperature, 300 K, in the region coloured in dark to ~600 K in the brightest one in the hotspot. It is worth remarking that thermal stationarity is reached quickly, within 1 s from the illumination of the film by the excitation beam (**Figure S3c).** One notices that, in absence of any other dissipation mechanism, the temperature reaches values well above the estimated temperature of the sample as determined by the hypothesis that blue shifting is caused by a high temperature, the temperature estimated by direct experiments, and also beyond the limit of the stability range of $MAPbI_3$. However, as also discussed in detail in the main text, the partially intact SEM imaging (**Figure S3a**) data suggest that part of the excess energy injected in the sample might go into forming ionic defects, which represents a fast and efficient dissipation mechanism that may prevent the film reaching very high temperatures and rapidly decomposing. In the main text, we discuss how the formation of defects gives a positive feedback by reducing the amount absorbed photons, hence of thermalisation energy to be dissipated, which improves the resistance of $MAPbI_3$ to light absorption-related thermal degradation processes.

In **Figure 2**, we discuss the dependence of the blue-shift of the PL peak as a function of the energy of the excitation source, which shows a linear correlation in the range between 1.8 eV and 2.5 eV (**Figure 2b**). We attribute this correlation to the increase of concentration of defects as a function of the energy of the excitation source: the higher is the energy of the photons, the higher is the thermalisation energy injected into the film, which is absorbed to create more defects. Here, we substantiate this idea investigating the trend of the temperature profile as a function of the photon energy in absence of any dissipation mechanism, *i.e.,* if there is no energy dissipation by Frenkel pairs formation. In **Figure S4**, we report the maximum temperature measured at three depth levels – 0, 0.25 and 0.5 mm from the top of the film – when the system has reached stationarity under illumination. One notices that there is a monotone, almost linear dependence of the maximum temperature on the energy of the excitation source and, as expected, the temperature is higher close to the absorption region (compare with **Figure S3b**). However, the temperature remains close to the absolute maximum, measured at the top of the sample, for a significant portion of the (computational) $MAPbI_3$ film, the difference with the top of the film being lower than 20K for half of the film thickness of more. Only near the interface with the glass support the temperature drops significantly, though it remains still rather high, higher than the measured one. The higher amount of thermal energy available in an extended region of the sample can be absorbed to create a higher concentration of Frenkel pairs of a large domain of the film.

The thermal model discussed above helps to establish the timescale of the recovery of a sample after irradiation has been stopped. As seen above, when the sample is irradiated with λ_{ex} = 450 nm photons it reaches a maximum temperature of 600 K if no other dissipation processes, such as formation of Frenkel pairs, act. Provided that the sample can transiently sustain such a high temperature, **Figure S3d** shows that within 1s the film recovers room temperature at all depth levels and any lateral distance from the focus point. Hence, as discussed in detail in the main text, high temperature is not the source of the persistent blue-shift when illumination is interrupted in the PL microscopy experiments with resting time in the dark.

Note S3: Thermal Imaging & Temperature Correction

We operated the thermal camera in two modes where one acquired images at a frame rate of 200 fps, and the other at a much slower rate of 6 fps. The former mode was used to understand the thermal behaviour right after the sample was exposed to light. In all measurements, the laser was switched on well before the measurement began in order to allow it to stabilize. The beam was blocked and only once the acquisition had started, the beam was unblocked. **Figure S5a** shows how the temperature along a line drawn across the center of the illumination spot evolves in time.

The effective pixel size in the thermal imaging measurement is 24 x 24 μm^2, which is slightly larger than the illumination spot. A possible effect of this is that the temperature measured in the pixel at the center of the excitation spot may represent an average across an area where the excitation intensity drops substantially from its very center toward the edge of the pixel. To account for this error, we introduce an artificial pixel in the center of the line profile as demonstrated in **Figure S5b**. Thereafter, we apply the same asymmetric Voight function when fitting the PL peak, and find that this fit extends slightly above the measured value. However, we find that it is only a few degrees higher, thus there is little to no impact on our interpretation of the data. More importantly, when we apply the same correction for every measurement in time, we can see that the same trend of temperature dropping gradually is still present, with only a slightly elevated temperature (**Figure S5c**).

Note S4: Theoretical calculations

Frenkel pair defect formation calculation

The model of the absorption of excess thermal energy that we propose to explain the persistent blue-shifting is based on the non-equilibrium formation of Frenkel pairs. Initially the sample contains a statistical quantity of any kind of defect and the thermalisation energy of hot carriers provides the energy to form Frenkel pairs of iodide and methylammonium defects, the most common defects in halide perovskites.[11–13] This is confirmed by direct ab initio MD simulations, showing that at 800 K, a temperature in the range predicted by the thermal model discussed in the Note II (**Figure S3**), iodide Frenkel pairs form within picoseconds. This affects the physical conditions of the sample, absorbing part of the thermal energy, which results in a reduction of the temperature of the sample. As shown in the main text, the increasing concentration of Frenkel pairs brings to the widening of the optical band gap and the reduction of the absorbance at any wavelength, which reduces the amount of photons absorbed by the film and the thermalisation energy, the difference between the energy of the photon and the bandgap. Thus, the dual effect of formation of Frenkel pairs - extraction of excess thermal energy and reduction of absorption of additional thermal energy - provides a positive feedback resulting in a self-regulating photoprotective mechanism preventing, to some extent, degradation of halide perovskites exposed to intense energetic excitation sources.

Undoubtedly, since the sample is not in equilibrium conditions, the thermal energy is not determined by the contact with a thermostat but by the injection of thermalisation energy of hot carriers created by the absorption of light emitted by the excitation source. Thus, one cannot determine the concentration of Frenkel pairs χ_D formed during the experiment by the usual Boltzmann distribution, $\chi_D = exp[-\Delta E_V / k_B T]$, where ΔE_V is the formation energy of the defect, *e.g.* a Frenkel pair of iodide or methylammonium. In fact, in the non-equilibrium conditions of our experiment, the thermal energy subtracted by the system to create a Frenkel pair results in a reduction of temperature. Frenkel pairs formed by this mechanism might recombine, re-injecting the corresponding thermal energy in the film, or split, driven by diffusion associated to their excess concentration in the hot spot and by long range attraction by grain boundaries.[3,14]

To investigate the efficiency of defects to absorb the thermal energy injected in the sample by thermalisation of hot carriers, we determined the energy formation of Frenkel pairs by *ab initio* molecular dynamics. In fact, recent computational works[15,16] have shown that since halides perovskites are soft materials the static picture of defects is inadequate at representing their properties. However, for reference, we also computed the formation energy of Frenkel pairs starting from the optimal crystal geometry. To go beyond the static picture, we performed extensive *ab initio* MD simulations of the bulk sample, *i.e.* without defects, and samples with iodide and methylammonium Frenkel pairs at various distances between them (**Figure S6**). The energetics of these samples is reported in **Table S1**. One notices that forming a methylammonium Frenkel pair at 300K costs ~3 times than the corresponding pair of iodide defects, when defects are at relatively short distance, with 2-3 perovskite pseudo-cubic unit cells. For the static picture, where it is possible to reliably eliminate the spurious interaction between periodic images of the point charges associated to defects, we computed also the formation energy of complementary Frenkel pair defects at large distance, denoted by ∞ in the table. In this case, the Frenkel pairs formation energy is almost the same, ~ 1eV. Our explanation for this energy difference is that MA^+ interstitial and vacancies strongly deform the lattice and this stress is released while they are separated. Thus, the energetic costs of separating methylammonium defects of opposite charge is partly compensated by the reduction of the stress on the inorganic sublattice. On the contrary, as stressed by several authors, iodide defects add little stress to the lattice and the energetic cost of splitting the Frenkel pair is not compensated by any sizable reduction of stress.

As can be seen in **Table 1**, the relatively flat energy profile of the Frenkel pairs as a function of the distance, as determined by the limited separation range that can be determined by simulations, suggests that complementary defects may not recombine immediately, thus permanently subtracting the associated excess thermal energy from the sample. It is worth remarking that i) the higher defects concentration in the hot spot brings to defects diffusion toward the rest of the sample, where defect concentration is lower. Moreover, ii) our recent works[3,14] have shown that grain boundaries can help separating complementary defects, further reducing the possibility of immediate recombination of defects and return of the corresponding thermal energy to the system. Finally, one has to consider that the free energy profile as a function of the distance between a vacancy and associated interstitial forming a Frenkel pair is even more flat than the corresponding energy profile (**Figure S7)**. In fact, the free energy is obtained by adding to the energy reported in **Table S1** the configurational entropic contribution to the free energy $-\mathrm{k}_B T\, log(\mathrm{N}_F)$, associated to the number N_F of sites with the prescribed distance between the defects forming a Frenkel pair. Since N_F scales with the square of the distance between the Frenkel pair, R_F, the corresponding entropic contribution to the free energy scales with $log(\mathrm{R}_F)$.

Finally, we also considered the case of Frenkel pairs in high defective samples. We determined the energy required to form a second iodide or methylammonium Frankel pair in a computational sample already containing a Frenkel pair of the same kind (**Table S1**). We observe a significant increase of the formation energy for both kind of defects but the effect is especially pronounced for iodide Frenkel pairs, which increases ~4 times with respect to the reference case.

Structural changes due to defect formation

We further employed molecular dynamics to calculate the indirect effect of defect formation on the material structure containing lower defect concentrations than ones used in the previous section. The analysis focused on four types of point-defects: interstitials (iodine I_I or methylammonium I_{MA}) and vacancies (iodine V_I and methylammonium V_{MA}). For each type of defect and for each defect concentration an atomistic model is generated by inserting randomly the corresponding number of defects (ranging within 1-100) in an equilibrated perfect crystal of 256 formula units. Though randomly distributed, defects satisfy the constraint to be maximum one per Pb_6^{4-} octahedra. For each defected $MAPbI_3$ crystal, it is performed a short dynamics of 4 ps, necessary to optimise the positions of atoms interacting with defects and to relax corresponding forces made relatively high due to the random insertion. After the relaxing stage, the dynamics continues at room temperature for 20 ps and the results are collected during the last 10 ps. The r_{off} offcentering is calculated during the last 10 ps.

Effect of defects concentration on the pseudo-cubic lattice parameter

Structural instability is observed for 3% iodine interstitials, 12% MA interstitials, 12 % iodine vacancies, 23% MA vacancies as can be seen in **Figure S8**. This ordering is likely dominated by electrostatic effects. In real conditions, positive and negative point defects form simultaneously and reduce electrostatic repulsion.

Effect of the defects on the Pb off-centering

The Pb off-centering is the distance (averaged during the dynamics) between the Pb atom and the centre of mass of the octahedra formed by the six-nearest neighbouring iodine atoms; the analysis is performed only on perfectly coordinated Pb atoms (*i.e.* complete perfect octahedra). In this way, we aim at mimicking the effects of defects on the bulk material. All defects affect the Pb off-centering by inducing an almost linear dependence on the concentration. All the defects also give rise to an asymmetric distribution of off-centering within the crystal that broadens and shifts with defect concentration. We focus on the displacement of Pb from the centre of Pb_6^{4-} (pristine octahedron), r_{off}, which Fabini *et al.*[17] have shown to induce changes in the bandgap of perovskites.

The behaviour of investigated defects (interstitials of MA and I and vacancies of MA and I) are qualitatively similar to each other. Each defect is characterised by a specific relation between defects concentration and off-centering but an almost linear dependence can be found approximately in all cases. **Figure S9** shows the distribution of r_{off}, or the probability of "off-centering". The peak of the distribution is at ~0.25 Å, in agreement with literature.[17] With increasing defect concentration the peak shifts toward higher off-centering and the distribution becomes broader. Subsequently, to identify the change in bandgap due to structural change, DFT calculations are performed on the bulk at PbI_3 sublattice configurations with the average off-centering r_{off} corresponding to the given defect concentration shown in **Figure S10** to examine the indirect effect of defects on the electronic properties of $MAPbI_3$. These calculations show that defects in $MAPbI_3$ lattice produce a blueshift of the PL peak, and that the amplitude of the shift, tens of nm, is consistent with the experimentally observed PL peak shift. We remark once again that the PL blue-shift discussed here is an *indirect* effect of defects *via* their perturbation of the structure of the PbI_3 sub-lattice of $MAPbI_3$ compared to *direct* effect seen in **Figure 2c**. Note that these calculations are also consistent with the mechanism proposed for vacancies, *i.e.* the defects induce a blue shift of the emission that can be modulated by their concentration.

Note S5: Structural changes upon light exposer at moderate flux

To investigate how the lattice parameters change during the measurement, we calculated pseudo-cubic *a* and *c*, *i.e.* the tetragonal lattice parameters determined from the 220 and 004 reflections, respectively, were transformed according to the group-subgroup relationship with $a_c = a_t/\sqrt{2}$ and $c_c = c_t/2$. As can be seen in **Figure S11**, the lattice parameters (pseudo-cubic *a* and *c*) change abruptly when illumination is on, which appears to be fully reversible as parameters jump back to the same values as before the illumination when light is off. However, the case for parameter *c* is more complex, as the reversible light induced effects appears to be superimposed over a non-reversible effect that causes *c* to shrink almost linearly with time. Given the WAXS experiment is performed under high vacuum conditions, and with synchrotron radiation, we considered this effect on our sample. We note in work by Hoye *et al.* that continuous irradiation by a synchrotron beam of higher energy (10.995 keV) and 20x larger flux in inert conditions was found to reduce the perovskite 110 scattering intensity by ~1% after 3800 s.[18] From this we conclude that at the lower beam dose used here, beam damage alone cannot account for the loss of scattering intensity during the experiment. In other work by Steirer *et al.* at a more comparable flux (1.5×10^9 photons s^{-1} mm^{-2}) but under ultra-high vacuum (2.67×10^{-9} mbar), a continual loss of iodine and deprotonation of methylammonium was observed in photoelectron spectroscopy measurements.[19] Therefore, the ongoing contraction of the pseudo *c* parameter over the whole measurement could be related to a gradual loss of volatile compounds, such as CH_3NH_2 or I_2. Note that during illumination, the pseudo-cubic *a* and *c* are unequal meaning there is no cubic formation at this point (more details of the transition in later part). However, after the illumination is switched off, the *c* parameter continues to linearly decrease, whereas at this point the *a* parameter starts to increase. We hypothesise that this observation relates to the formation of isotropic structure due to presence of defects as also mentioned in the main text.

We further analysed the data to understand this behaviour as the light is switched off. As a Rietveld refinement of the two apparently cubic/isotropic and tetragonal structures was impossible due to the restricted angular range of the WAXS data, instead, we estimate the phase ratios using the areas of the fitted 004/220 reflections of the tetragonal phase, together with the emerging 200 reflection of the isotropic phase (**Figure S12**). As both phases have similar scattering length density – mainly determined through the lead content – this simple comparison yields reliable estimates of the phase fraction. Further, we fit the kinetics with a Johnson-Mehl-Avrami-Kolmogorov type function (JMAK) as would be expected for solid state transitions, an approach which has been used to model crystallisation/solid formation process in halide perovskite systems.[20]

$$f(t) = 100\%\cdot\exp[-k\cdot(t-t_0)^n]$$

for the diminishing tetragonal phase and

$$f(t) = 100\%\cdot(1-\exp[-k\cdot(t-t_0)^n])$$

for the appearing isotropic phase. This fitting (**Table S2**) most importantly allows us to estimate the starting point t_0, at which the isotropic phase begins to arise, with $t_0 = 97\pm4$ min (relative to the start of the experiment). This is, in fact, immediately after the light is turned off and not during the illumination itself. Hence, this analysis precludes the possibility that the final structure is due to a purely thermal transition. This also suggests that while defects are formed during illumination, the volatilisation process in vacuum described above is partially inhibited during illumination.

Therefore, we propose that the structure emerging due to illumination is an isotropic structure due to defect formation and the removal of volatile species in UHV condition. As the defect population increases, the lead halide octahedral structure is less constrained, resulting in the tetragonal phase becoming less distorted, leading to an overall more isotropic cubic-like structure, as evidenced by cubic-like 200 and 100 reflections. We note that in **Figure S11**, the 004 reflection has higher intensity compared to 220 reflection, which is unexpected in a random oriented polycrystalline material. There are several reports have shown that this ratio of 004/220 strongly depends on the ratio between MAI and PbI_2 as well as the used substrates.[21,22] Although we do not have explanation for our case, we expect negligible contribution of this orientation to the observed phenomena.

Note S6: Additional Raman spectra and calculated vibration modes

To understand how the light induced structural changes, we further employed Raman scattering with wavelength of 532 nm (2.33 eV). The excitation power density is 150 kW/cm^2 to measure the initial and recovery state whereas 5 times higher power density (750 kW/cm^2) is used to degrade the sample. The sample is $MAPbI_3$ thin-film on glass substrate, which was put inside a sample holder with a continuous flow of N_2 attached with a temperature controller. The temperature of the sample is estimated from the temperature of the N_2 flow, hence, the actual material temperature in the experiment can be slightly higher. Note that the sample is exposed to air for about 5 minutes before mounting in the sample holder of the Raman setup.

Figure S16 exhibits different vibration modes of $MAPbI_3$ in the presence of different types of defect. Note here that vibrational modes can be Raman inactive, hence, molecular dynamics calculated spectra can be different from experimental obtained Raman spectra. The MD curves are normalised to the same integral over the whole domain frequency. Although MD force field can only be qualitative, the evolution of calculated spectra with defect can give some insights into the reason behind the changes in Raman spectra before and after degradation shown in **Figure 4** in the main text. In particular, data presented in **Figure S16** show that at very high defects concentration the structure undergoes “amorphization” with a qualitative change in the spectrum. For all type of defects, there is a reduction of the peak within 300-400 cm^{-1} that seems to be consistent with experiments. Moreover, MD shows that the disappearance of this peak does not require the out-diffusion of the molecules since also MA interstitials and iodine interstitials can produce a similar trend; rather MD indicates that the evolution of the peak in the short wavenumber range can be due to an average disordering of the Pb-I structure. Hence, this supports the involvement of MA and I defects on the changes in Raman spectra due to photon-induced degradation.

Note S7: Effect of different excitation wavelength to the degradation pathways

To understand the effect of lower energy photons on the film, we exposed the $MAPbI_3$ film to red light (637 nm, 1.95 eV) with an excitation density around 3.1 kW/cm^2 (30,000 Suns) for two minutes. After exposure, PL signals from both PbI_2 (~510 nm or 2.43 eV)[23] and $MAPbI_3$ (~790 nm or 1.57 eV) are detected (**Figure S19a**). Moreover, in the excited spot, the $MAPbI_3$ had a broad high-energy shoulder, which we attribute to a high ionic defect concentration and increased structural disorder - consistent with our results discussed above and previous reports.[24,25] The relative PL intensity of the PbI_2 peak with respect to the $MAPbI_3$ peak decreases the further away from the irradiated spot we measure, while the $MAPbI_3$ emission peak simultaneously becomes less blue-shifted.

Exposing the films to blue light as in **Figure 1**, but for 120s instead of just 15 seconds, $MAPbI_3$ emission is observed, albeit at lower intensity. Of more importance is that no PbI_2 emission can be found (blue trace in **Figure S19a**), suggesting different degradation species between red and blue excitation. Energy dispersive X-ray (EDX) maps of Pb and I of the regions exposed to both red and blue light in **Figure S19b** show a reduction of I in both the exposed regions. For Pb, however, there is quite interestingly an increase in the signal after excitation with blue light, which suggests that the intense excitation induces the formation of additional Pb-related species, most likely Pb^0 (also previously observed)[26,27] resulting in a strong Pb signal in the EDX image. On the other hand, the sample irradiated with red light shows no change in Pb signal, which is in line with the formation of PbI_2 rather than Pb^0, which is also supported by the PL measurements. Thus, in the case of high energy photons it is likely that the first step involves the formation of PbI_2, after which a transformation from PbI_2 to Pb^0 occurs since photons have sufficient energy (2.76 eV). Hence, this two-step process could be explained by the combination of photo-dissociation and thermalisation resulting in the breaking of the Pb-I bond discussed in the main text. Meanwhile, excitation at 1.95 eV is insufficient to absorb in the PbI_2, although it is still sufficient to produce ionic defects in the perovskite. Moreover, as the bandgap shifts to higher energies with more defects, the self-regulating photoprotective mechanism prevents excitation at lower photon energies to degrade the perovskites any further than into PbI_2.

Note S8: Maximum power point tracking under concentrated sunlight

A Fresnel lens with a diameter of 10 cm was used to concentrate simulated sunlight onto a set of devices. The flux was estimated to reach a maximum of 3.5 Sun. The devices were not placed at the optimal focus in order to illuminate more than once cell. **Figure S20a** shows the experimental setup. We obtained a stable normalized efficiency for 18 hours (**Figure S20b**).

Note S9: Effect of different photon energies on the device degradation

The discussion until now indicate that depending on the photon energy, defect formation in $MAPbI_3$ can undergo different pathways. In short, the blue photon with higher photon energy than 2.45 eV can induce photodissociation, which directly break Pb-I bond forming Pb^0. Though it has been reported that $MAPbI_3$ can form from Pb^0 while exposing to polyiodide melts - not likely to happen in operational conditions.[28] Hence, it is expected that the material can have higher degree of recovery in the dark when exposing the photoenergies below PbI_2 bandgap.

To understand the practical implications of present results on perovskite solar cells, we fabricated p-i-n architecture $MAPbI_3$ devices (see **Figure S21** for initial efficiency) and subjected them to different parts of simulated global AM1.5 solar radiation using bandpass filters with central wavelengths at 470 nm and 635 nm (30 nm bandwidth for both). For simplicity, we will refer to these two identical devices as 'blue' and 'red' devices respectively simulating the effect of day-night cycling. The cell structure is p-i-n consisting of ITO/PTAA or SAM/Perovskite/C60/BCP/Cu. Here, PTAA stands for poly[bis(4-phenyl)(2,4,6-trimethylphenyl)amine], SAM is self-assembled monolayer as the hole selective layer previously reported,[29] BCP stands for bathocuproine. We chose to use different hole selective layers to make sure the result is independent of the perovskites grown on different substrates.

Both devices initially exhibit some degree of enhancement before stabilising for a few diurnal cycles. Once some degree of degradation is detected, we measure J-V curves after a 12-hour period of light soaking, and also after allowing it to rest for 8 hours. As can be seen in **Figure S22a-b**, degradation of the blue device is quite extensive and providing it to rest in dark does not recover its efficiency. The red device, on the other hand, improves beyond its initial values despite showing signs of degradation after light soaking, which is also apparent in its normalised diurnal efficiency in **Figure S22c**. **Figure S22d** shows that the V_{OC} decreases significantly for the blue device in the period of 7 day-night cycling. However, V_{OC} drastically improves for the red device with rest and seems to rely on the dark period for stabilising the V_{OC} and efficiency. As V_{OC} is the device parameter most directly related to defects of the absorber,[30] it aligns well with notion that defects generated with sufficiently low energy can recover given time to rest. In connection with previous results on the recovery of the absorber using Raman spectroscopy (**Figure 4**), these results suggest that the phenomenon is connected with the formation and recovery of MA and I-related defects. The seemingly irreversible degradation observed for the blue device also supports the hypothesis of high energy photons forming Pb^0 from PbI_2 in agreement with previous discussion in SI note S7, which is assumed not to recover.

In the main text, we thorough examine of the relatively simple $MAPbI_3$ perovskite compound. To place our findings in a more technologically competitive framework, we repeated the diurnal filtered light soaking experiment on a device consisting of a state-of-the-art 'triple cation' ($Cs_{0.05}(FA_{0.83}MA_{0.17})_{0.95}Pb(I_{0.84}Br_{0.16})_3$ labelled as CsFAMA adapted from Saliba *et al.*[31]) perovskite absorber, which has become a standard device in the field with high efficiency and improved stability compared to $MAPbI_3$–based devices.[32] **Figure S21** show the initial device performance of all device architectures before aging experiments.

The J-V behaviours of CsFAMA are similar to $MAPbI_3$ (comparing **Figure S22** to **Figure S23**). However, unlike for $MAPbI_3$ cells, the parameters improve during day and return to initial values during night for much longer period (comparing 3 days for $MAPbI_3$ and more than 10 days for CsFAMA), which we attribute to the well-reported photon-enhancement or photobrightening phenomenon widely observed for perovskites.[33] While explanations of the mechanism behind photobrightening differ in their details, most agree that the phenomenon involves some process of defect annihilation.[34] **Figure S23** indeed shows large fluctuations of V_{OC}, which agrees with this notion. It is quite interesting that V_{OC} fluctuates in the CsFAMA device when exposed to the red part of the solar spectrum, while V_{OC} remains more constant when exposed to blue light; in other words, blue shows neither enhancement nor a recovery.

After 8 cycles we observe changing trends where the blue device starts to gently drop in efficiency. The red device, while maintaining a stable efficiency, starts to transition into a pattern of decreasing efficiency during light exposure and recovery in dark, which is more evident in the last two cycles. Hence, as the device enhancement dwindles, degradation becomes increasingly prominent and only then can recovery manifest itself. For the blue device, resting in dark does not provide a sustainable recovery and the device successively loses efficiency. For the red device, however, the dark period provides the necessary recovery for increased stability. While more extensive measurements are required, the goal here was to demonstrate that similar processes are likely at work in more complex perovskites, rendering the findings presented herein more general to perovskite compounds where photo-induced degradation and recovery has been demonstrated.[3,35–38]

Supplemental Figures & Tables

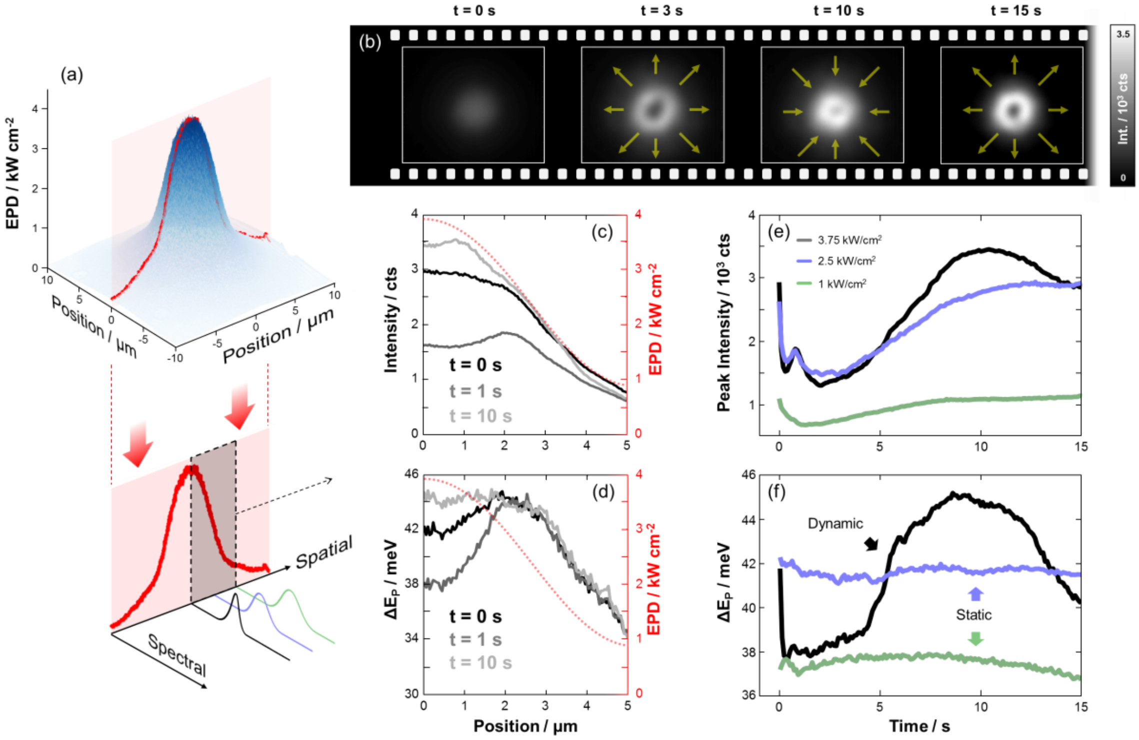

Figure S1 – Spatially and spectrally resolved PL at high photon flux. (a) 3D representation of the excitation spot converted into excitation power density (EPD). We look at a cross-section profile of the excitation spot (red plane) from which we extract a spectrum at every position demonstrated in the lower schematic. (b) Snapshot PL images of the spatially distributed PL at t = 0 s, 3 s, 10 s and 15 s. The evolution of (c) PL peak intensity and (d) PL peak energy extracted from the spectral fits over time and space shown for t = 0 s, 1 s and 10 s. (e-f) The peak positions at different positions for the duration of 15 seconds observed for different positions: at the centre of the excitation point (black traces), at the threshold of the peak shifts (blue traces), and at the tail of laser excitation profile (red traces).

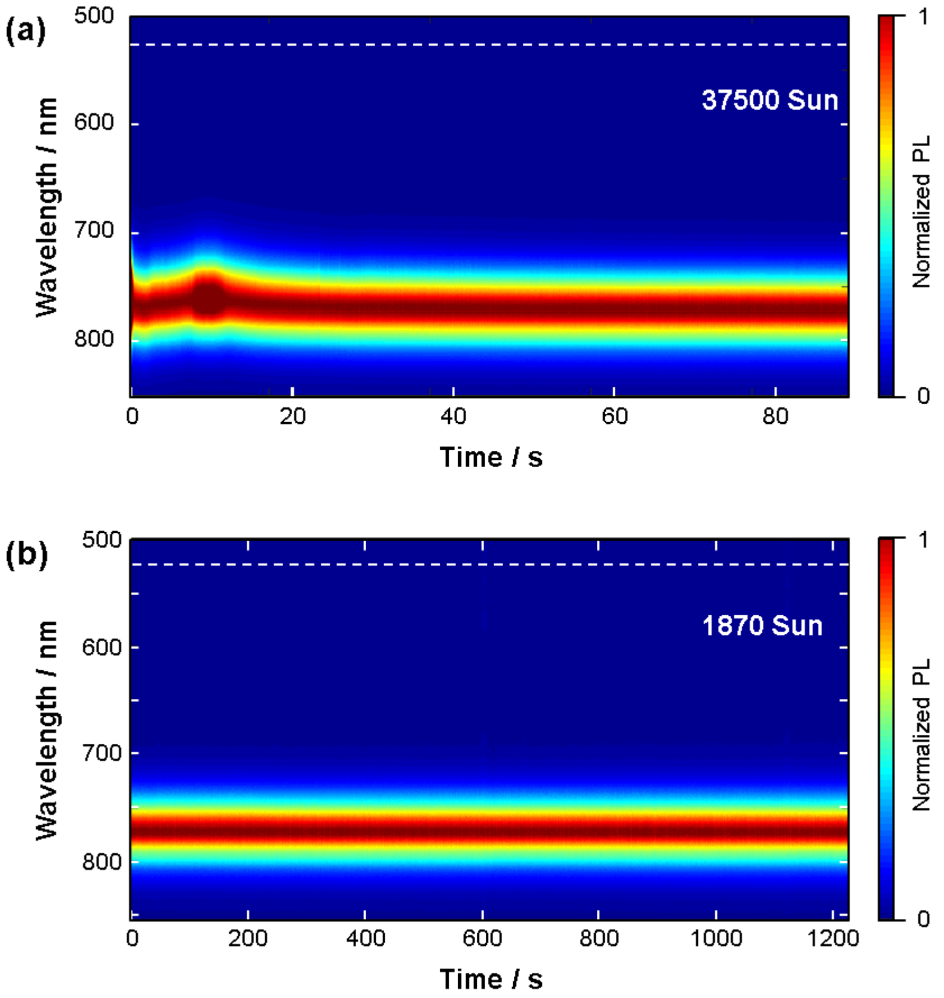

Figure S2 – PL peak evolution in time at high flux. (a) PL spectra heat map showing the time-evolution of the perovskite emission with absence of any emission indicating significant degradation into PbI_2 at (a) 37500 Sun for 90 seconds and (b) 1870 Sun for 20 minutes.

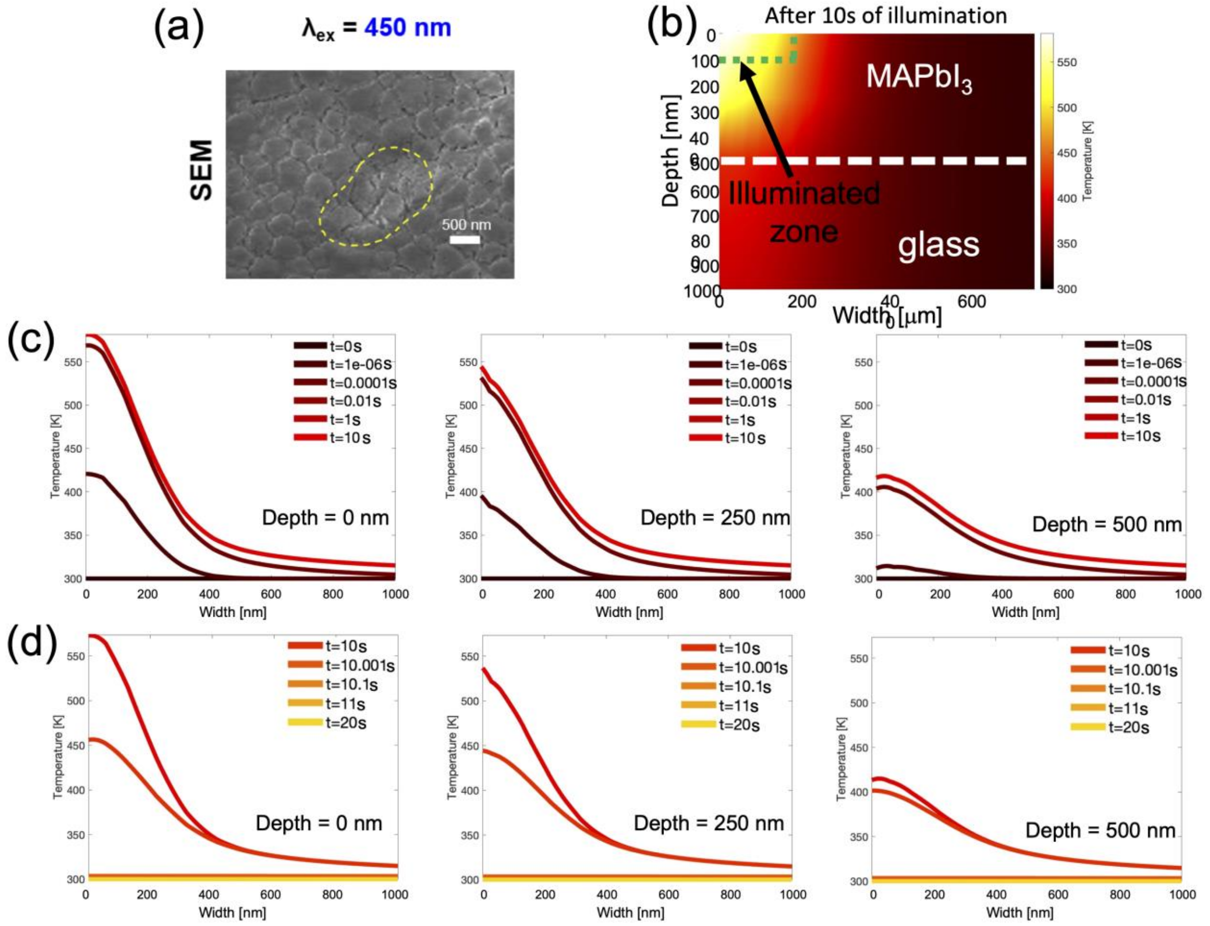

Figure S3 – Heat diffusion model under high photon flux. (a) SEM image of the irradiated region. (b) Colour map of the temperature of the sample at 10s after the beginning of illumination at 3.1 kW/cm^2 of light source at λ_{ex} = 450 nm (photon energy 2.75 eV). In the figure are also shown the various regions of the sample: i) the MAPbI$_3$ film - delimited by the white dashed line - with ii) a cylindrical region of width 2.5 mm and 0.1 mm, where (most of) the excitation light is absorbed – enclosed within the dashed green boundary - iii) deposited over a glass slab. c) temperature profiles at various times after the beginning of irradiation at several levels of depth in the MAPbI$_3$ film. d) Same as panel c) after irradiation has been stopped at 10 s.

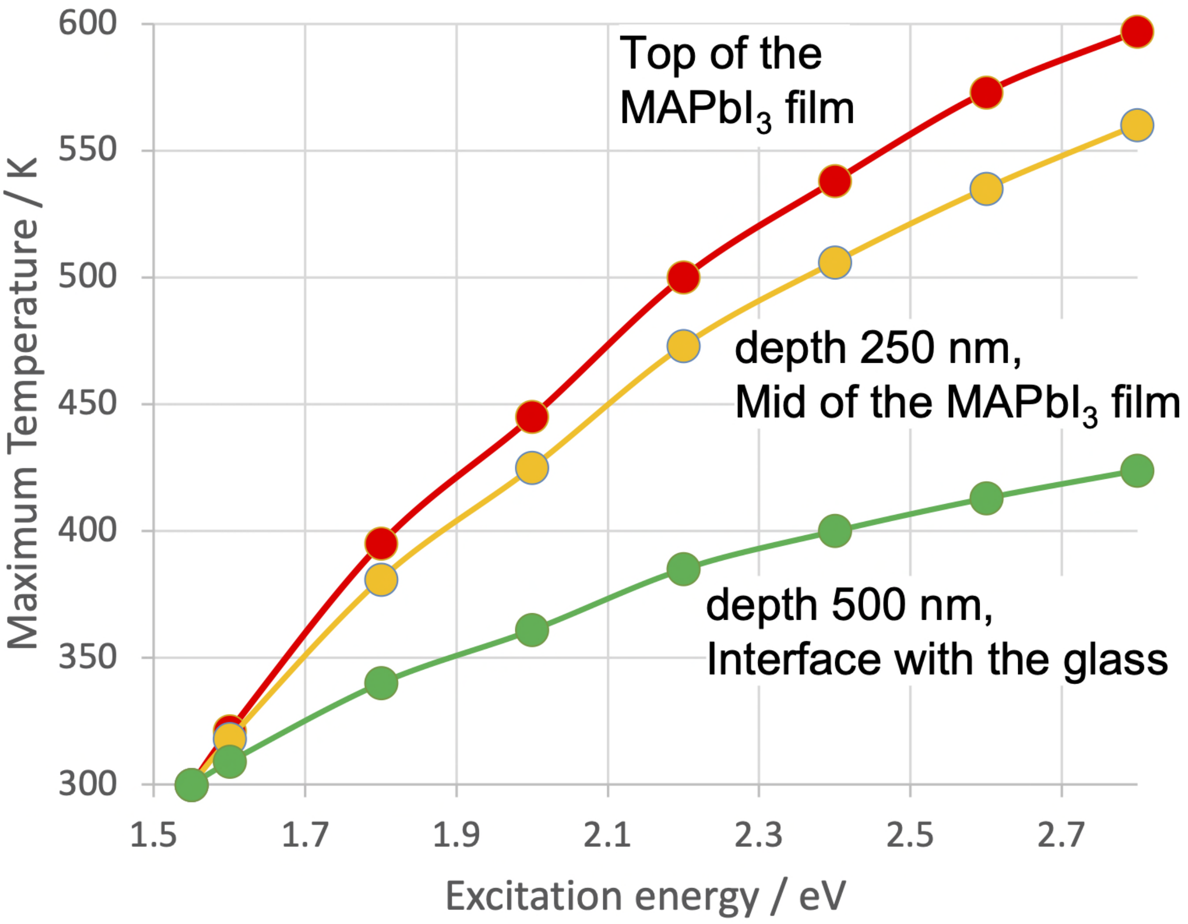

Figure S4 – Expected film temperature under illumination. Maximum temperature at depths 0 nm – top of the MAPbI$_3$ film, 250 nm- mid of the MAPbI$_3$ film and 500 nm - bottom of the MAPbI$_3$ film, at the interface with the glass support as a function of the photon energy of the excitation source. One notices that apart for the 1.55 nm (same as bandgap) and 1.6 eV cases, the temperature in the field is predicted to be significantly higher than the measured one, reaching, for the higher photon energies, MAPbI$_3$ degradation temperature.

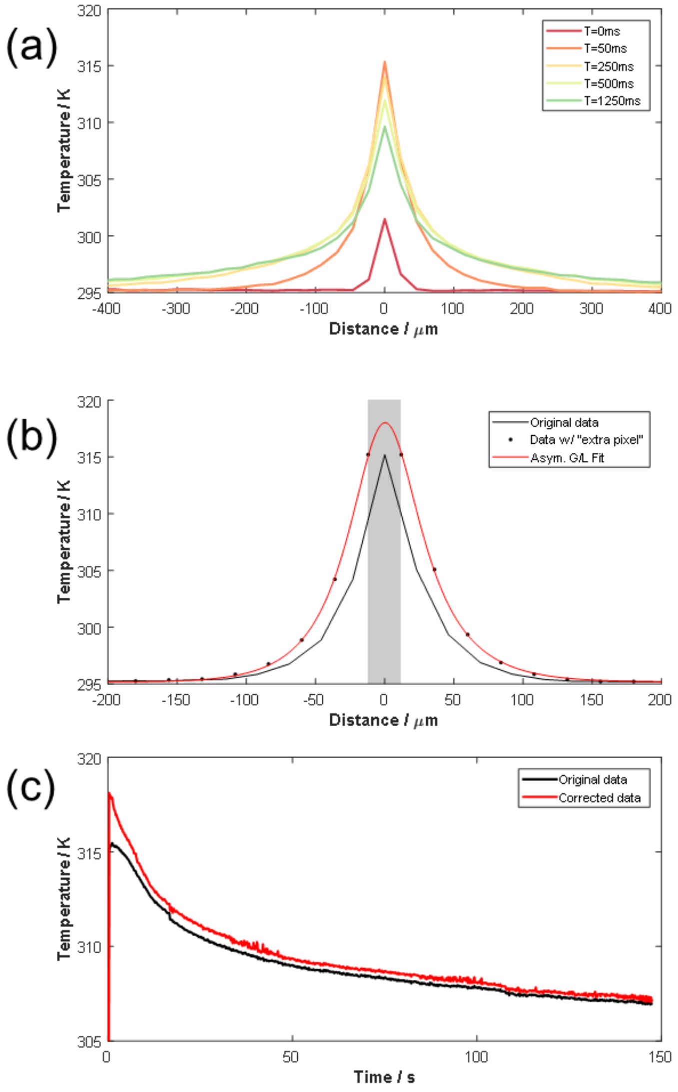

Figure S5 – Temperature under illumination measured as a function of space and time. (a) Temperature vs distance profile from the laser focus at several times after the beginning of irradiation at 30ksun. (b) The artificial scenario of inserting a pixel (black shaded region) in order to extrapolate through fitting an asymmetric mixed Gaussian/Lorentzian function to the data points and obtaining a peak value. (c) Measured (black) and corrected (red) temperature trends from data in Figure 1c of the manuscript.

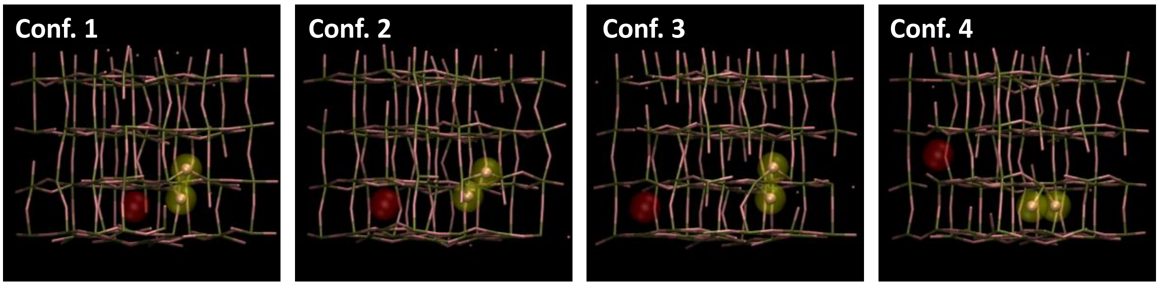

Iodide Frenkel Pairs

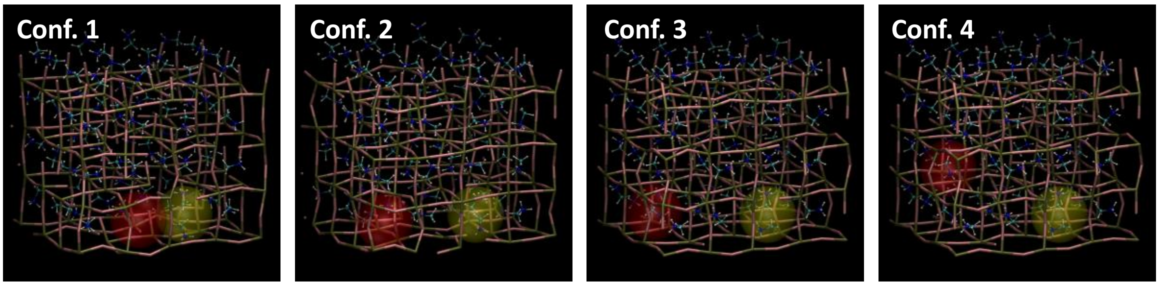

Methylammonium Frenkel Pairs

Figure S6 –$MAPbI_3$ Frenkel pair formation and dynamics under illumination. 300 K *ab initio* MD simulations have been performed starting from four different initial configurations corresponding to different distances between the iodide (top) or methylammonium (bottom) vacancy and interstitial defects forming the Frenkel pairs. Within the duration of the dynamics, 10 ps for each simulation, the defects remain at their initial positions. In the panels above, iodide and methylammonium interstitials have highlighted by yellow spheres and the corresponding vacancies by red spots. Configurations 1 to 4 are at increasing distance between the vacancy and interstitial defects of the Frenkel pair.

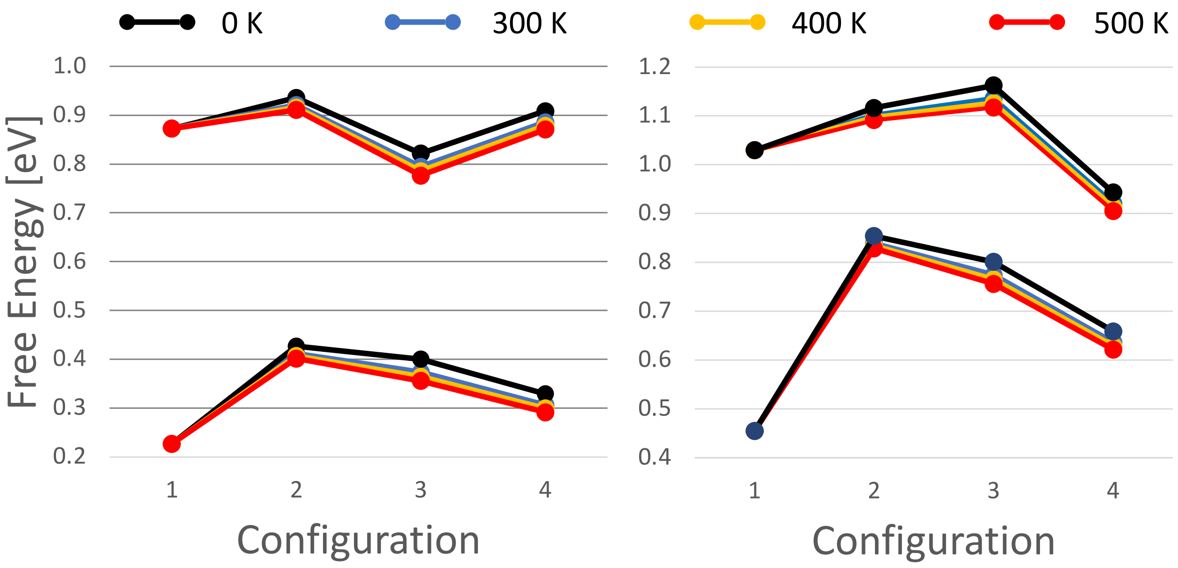

Figure S7 – Free energy profiles Frenkel pairs as a function of the vacancy-interstitial distance at various temperatures. Free energy profile of methylammonium (top) e iodide (bottom) Frenkel pairs as a function of the configuration at 0 (black), 300 (blue), 400 (orange) and 500 K (red). Data reported in the figure are obtained by the formation energy computed from geometry relaxation (left) and *ab initio* MD at 300 K (right). Corresponding data are reported in **Table S1**. With free energy we refer to the sum of the formation energy of a defect at a given configuration and the configurational entropic contribution at various temperatures, $-k_B T\, log(N_F)$. We remark that, in general, the distance, hence number of equivalent Frenkel pair configurations, grows in going from configuration 1, 2, 3 and 4. In the figure we did not report the case of separated defects, configuration ∞, as the corresponding free energy depends on the distance, which is not defined within the model.

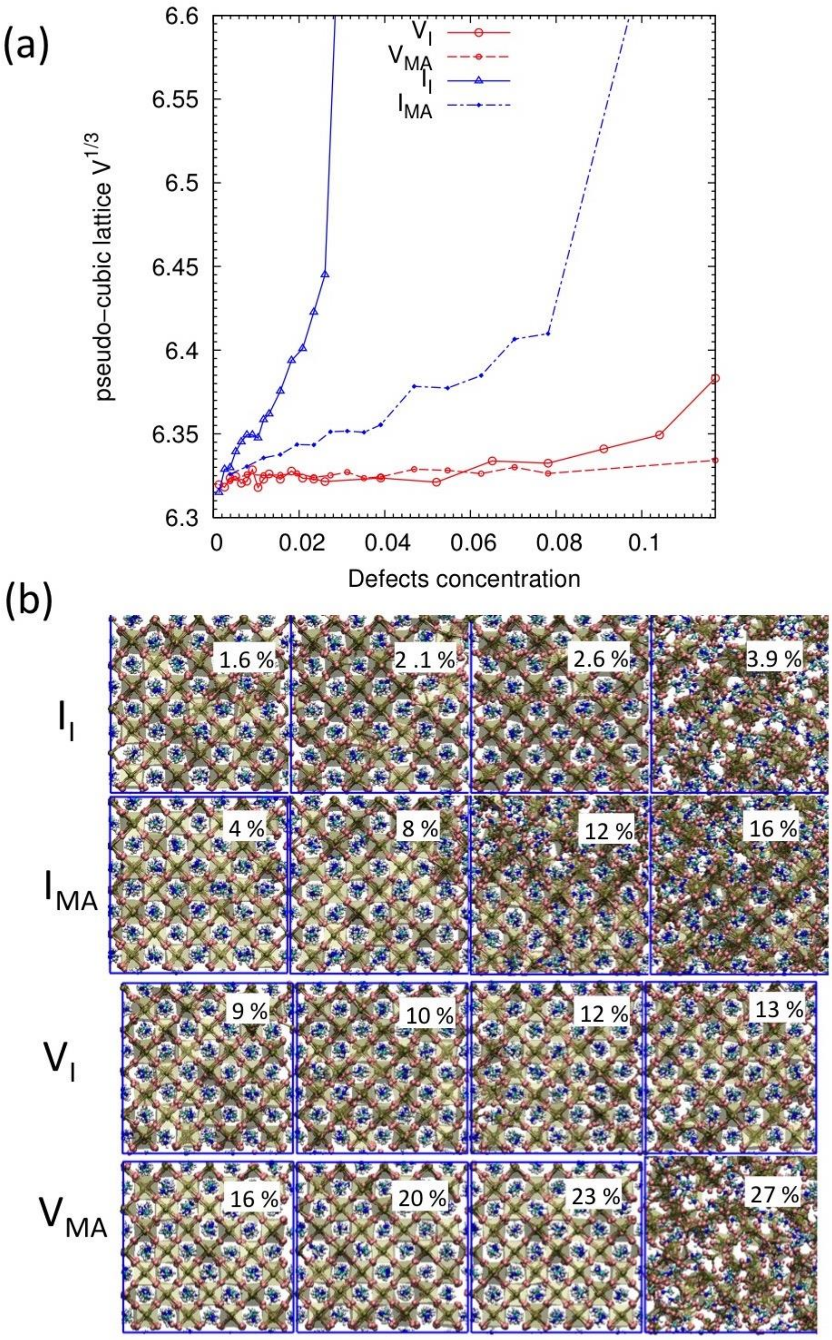

Figure S8 – Lattice deformation as a function of defect concentration. (a) The pseudo-cubic parameter of $MAPbI_3$ with different defect concentrations. (b) Snapshots of $MAPbI_3$ with different defect concentration. Compared to the pristine lattice, the lattice with defects gets more distorted as the defects form which increases the pseudo-cubic parameter.

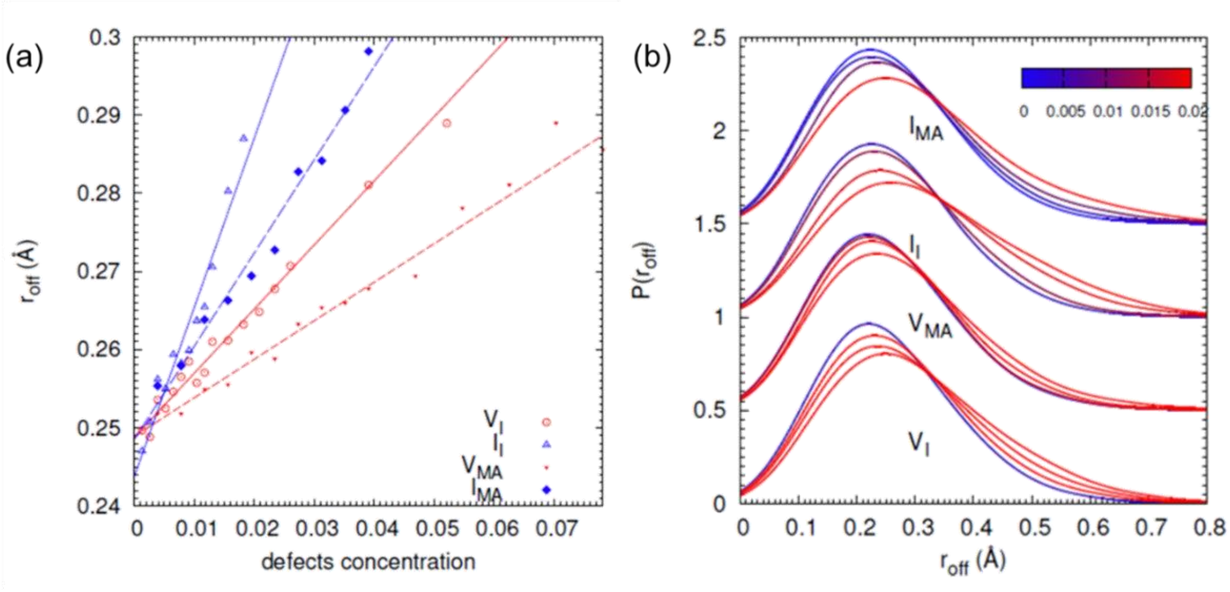

Figure S9 – Pb off-centering as a function of defect concentration. (a) The dependent of off-centering parameters on the defect concentration of different defects. (b) The probability $P(r_{off})$ of different magnitude of r_{off} for different defects.

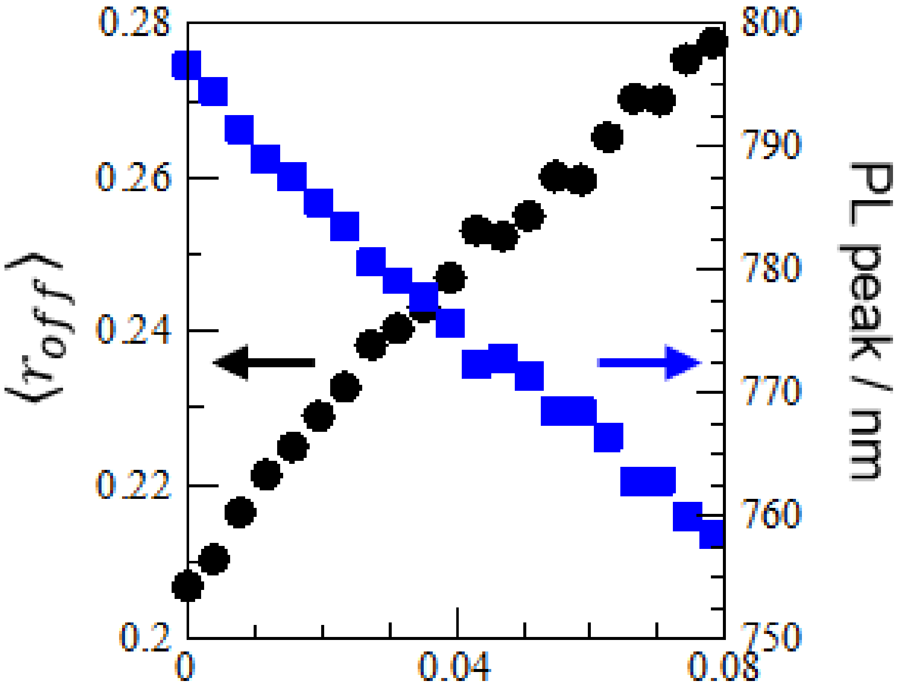

Figure S10 – Pb off-centering and PL peak position. r_{off} trend corresponds to the PL peak (bandgap) of the material.

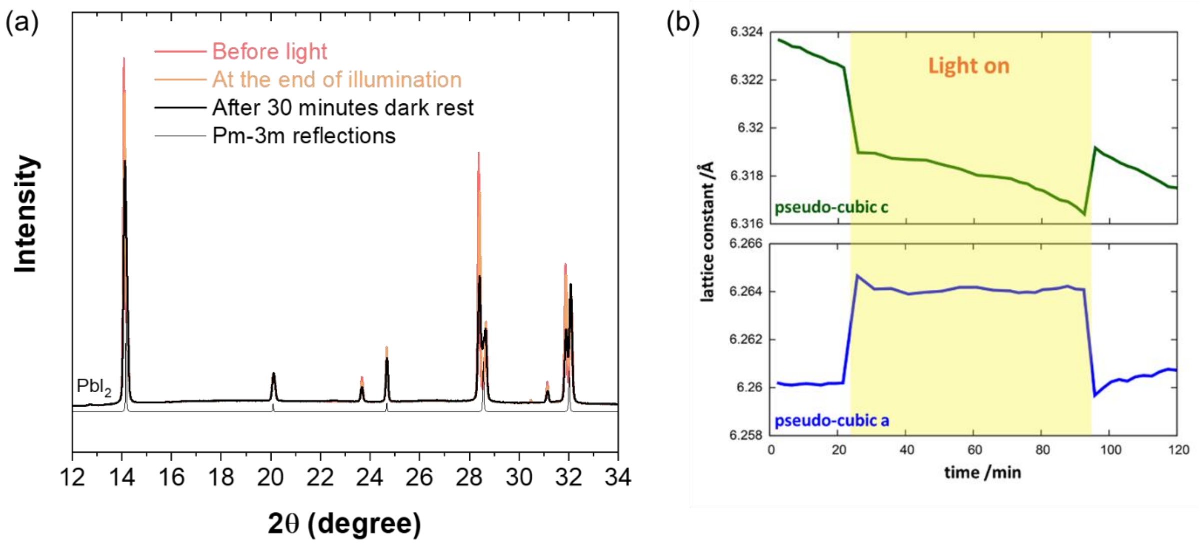

Figure S11 – Photo-induced structural changes at moderate flux. (a) Full 1D pattern of before illumination, at the end of illumination and after 30 minutes dark rest together with the 1D cubic $MAPbI_3$ structure calculated for unit cell of 6.283 Å. (b) Evolution of the pseudo-cubic lattice constants *a* and *c* as calculation from single peak fittings of the 220 and 004 reflections, respectively.

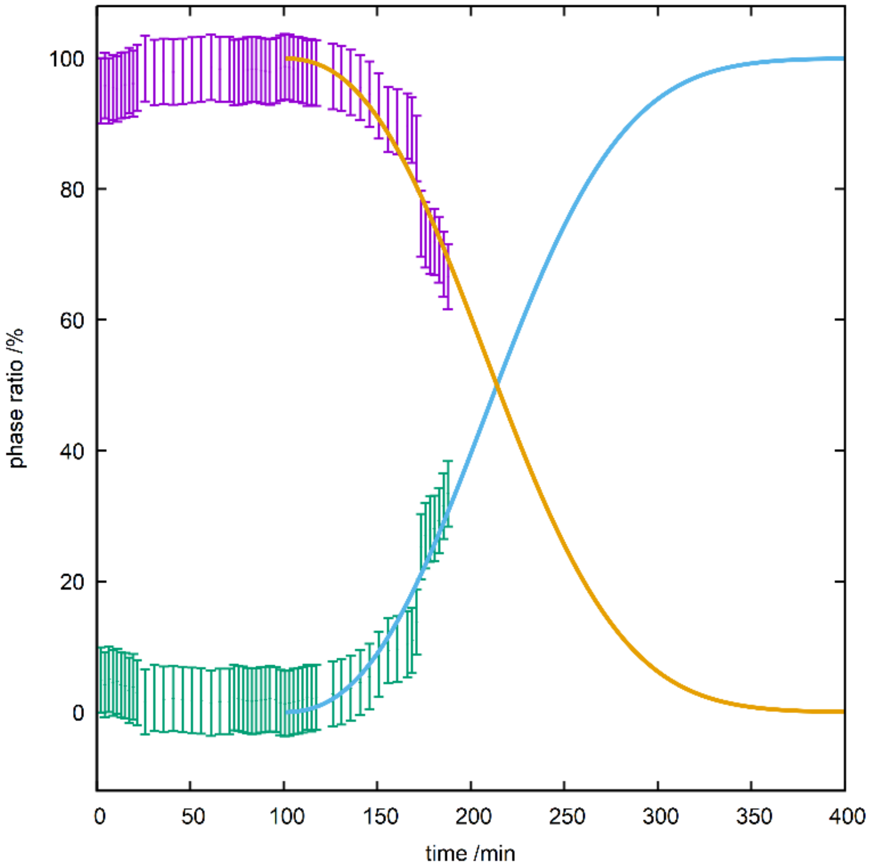

Figure S12 – Tetragonal and isotropic phase ratios as a function of time. Phase ratio estimations for the tetragonal phase (violet) and the isotropic structure (green) from single peak fittings together with Johnson-Mehl-Avrami-Kolmogorov-type kinetic fits (orange and blue respectively) for the phase transition. The error for the phase fractions is estimated to be of the order of ±5 %.

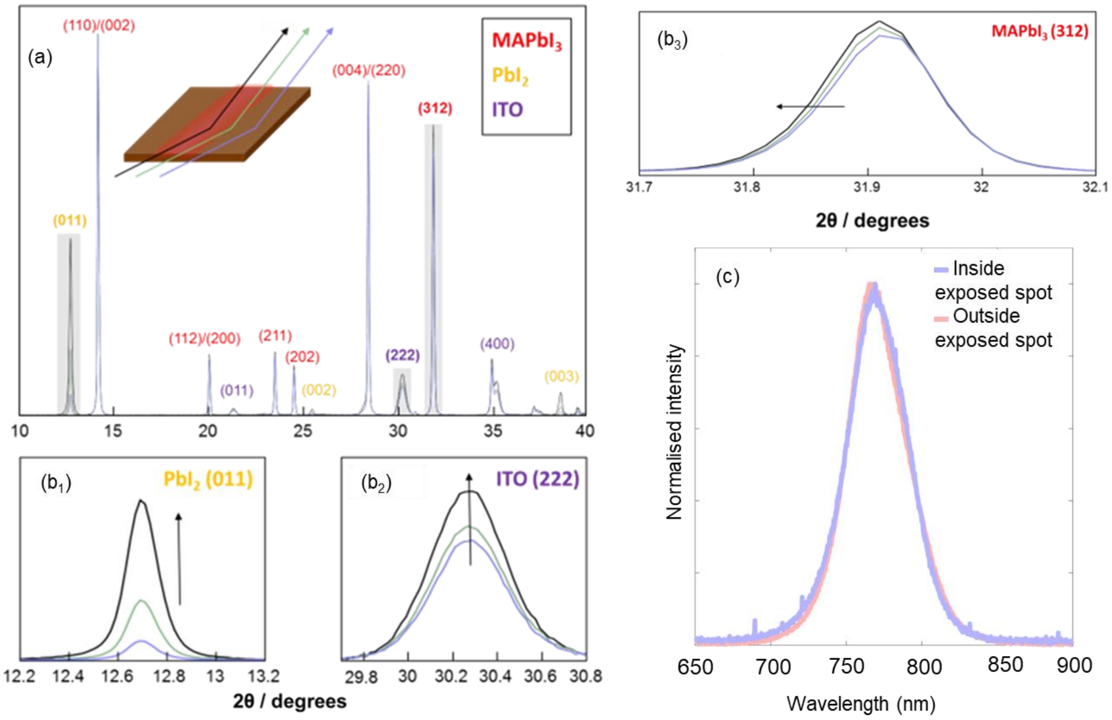

Figure S13 – Structural changes under intense flux for an extended time period. (a) Ex-situ GIWAXS diffraction patterns of thin film MAPbI$_3$. exposed to red light (λ = 637 nm, 300 sun for 5 hours). The black line is directly inside the laser exposed spot, green line is on the edge of the spot and light blue line is further away from the spot. (b$_1$) An increment of PbI$_2$ is due to degradation from MAPbI$_3$ in agreement with PL total spectrum in (c). The ITO peaks (b$_2$) exhibit no shift moving away from the laser spot though the intensity of the peak increases possible due to a thinner MAPbI$_3$ caused by the loss of MA (either by evaporating outside the film or migrating away from the laser spot). (b$_3$) The MAPbI$_3$ 312 peak shows a peak broadening towards lower 2θ angle. (c) The PL spectra of respective area.

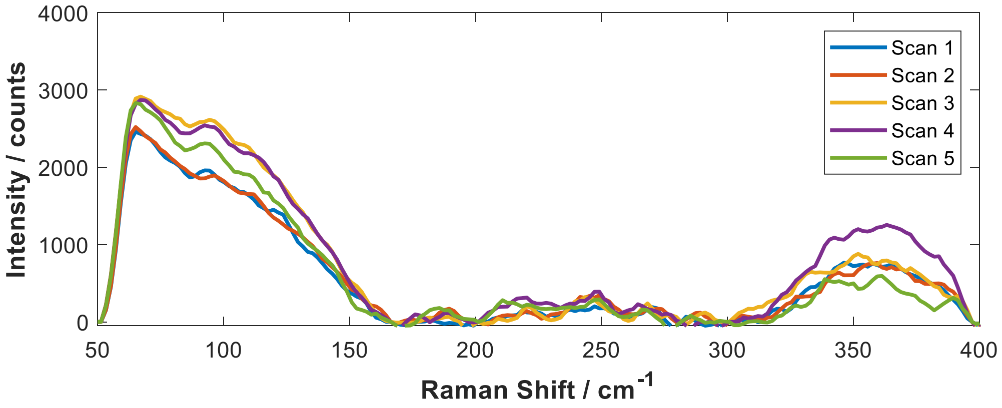

Figure S14 – Raman spectra for initial stability. Initial Raman spectra with repeated scans to determine the stability of the sample during the measurement.

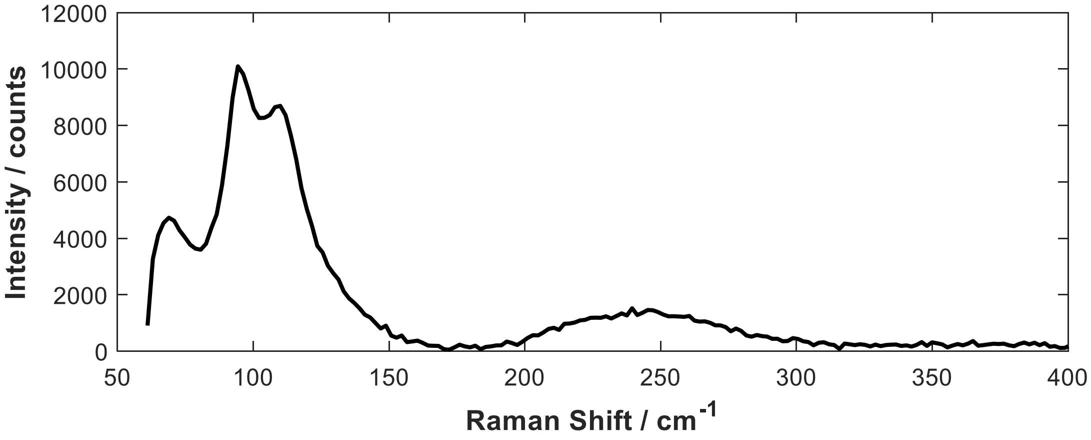

Figure S15 – Raman spectrum of PbI_2. The Raman spectra of complete degraded sample until PbI_2 (visible by the naked eye).

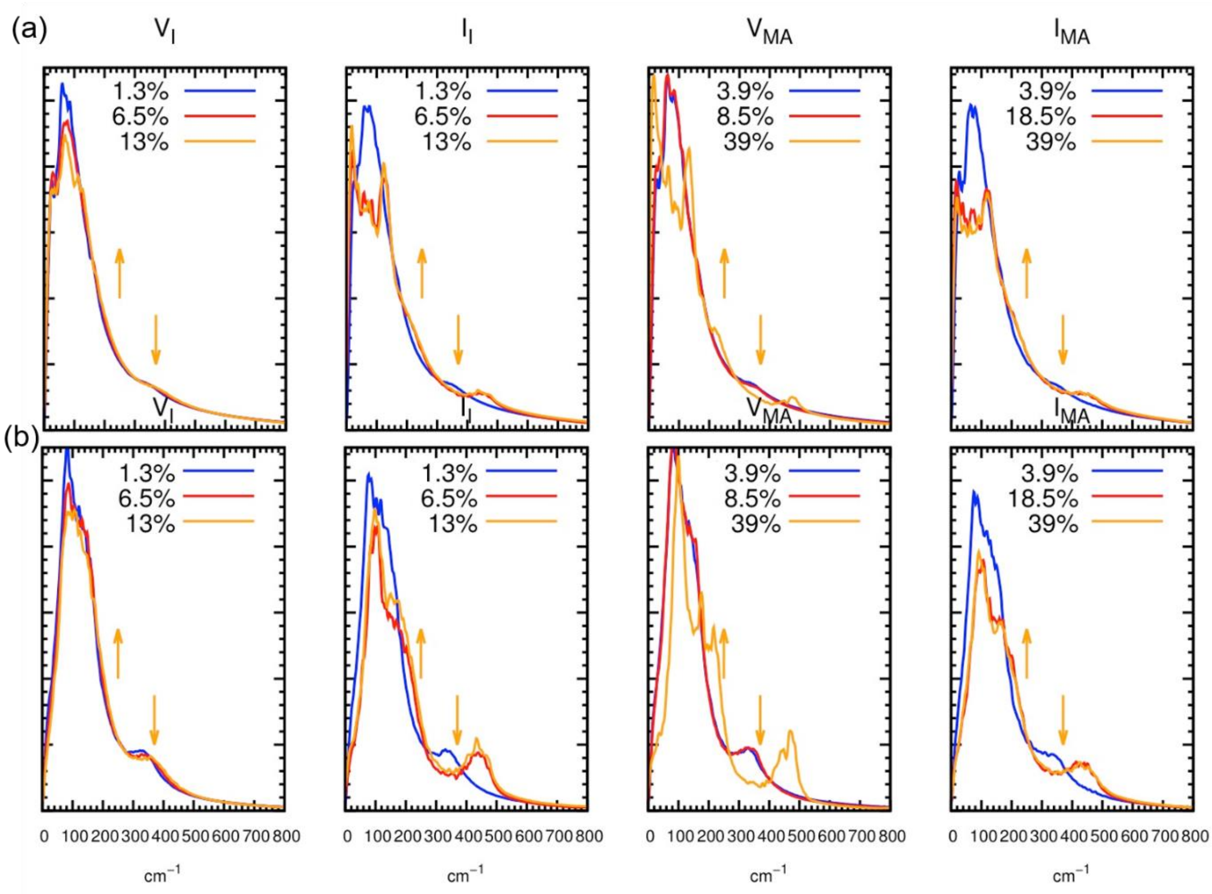

Figure S16 – Dependence of calculated MAPbI$_3$ vibrational spectrum on the presence of defects. (a) The vibrational MAPbI$_3$ spectra calculated for the four types of defect. (b) The same spectrum projected on molecules (there is an relative increase of heights of molecular peaks).

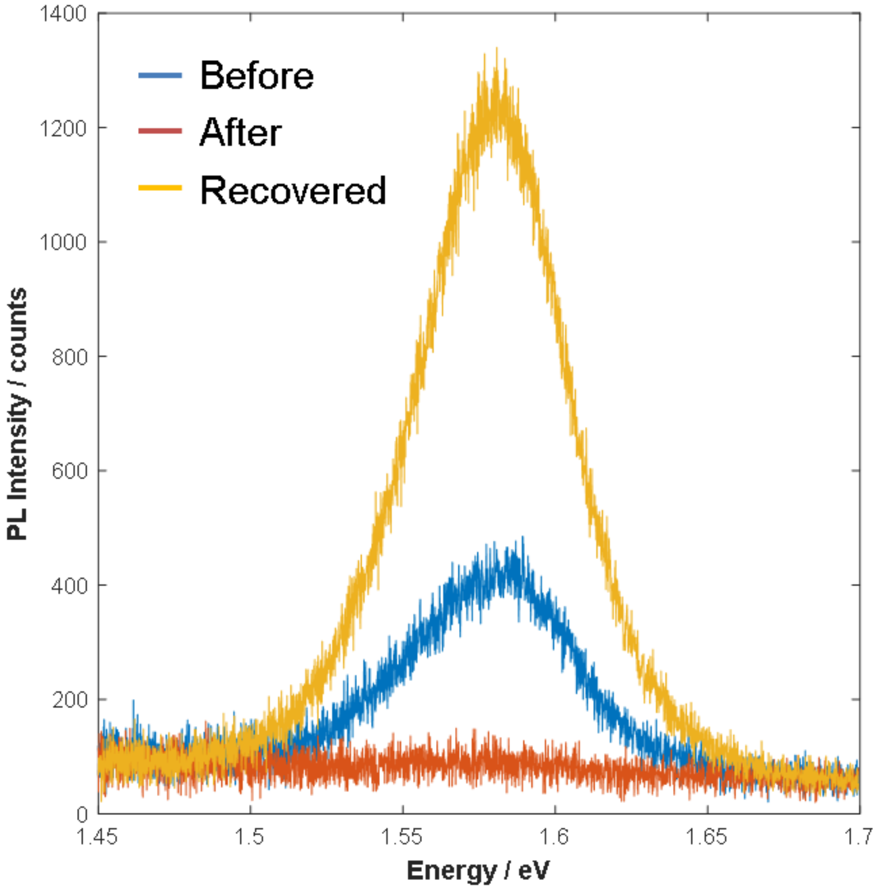

Figure S17 – PL spectra during Raman measurements. PL spectra collected before degradation (blue), right after degradation (red), and after recovery (yellow).

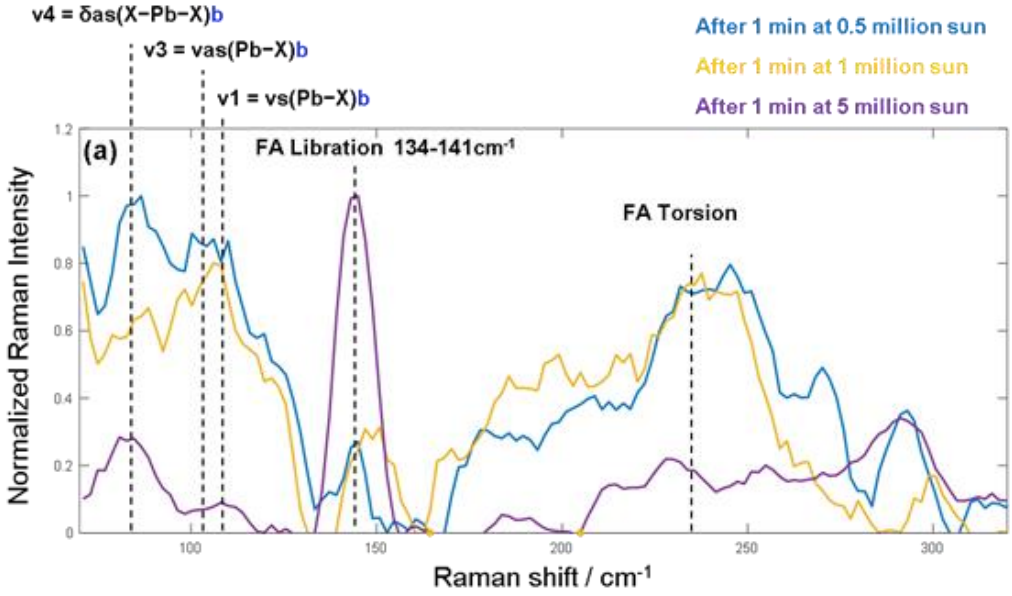

Figure S18 – Raman Spectra of $Cs_{0.15}FA_{0.85}PbI_3$. Raman spectra upon intense illumination at room temperature. Vibration of mode assignment follows reports in literature.[39,40]

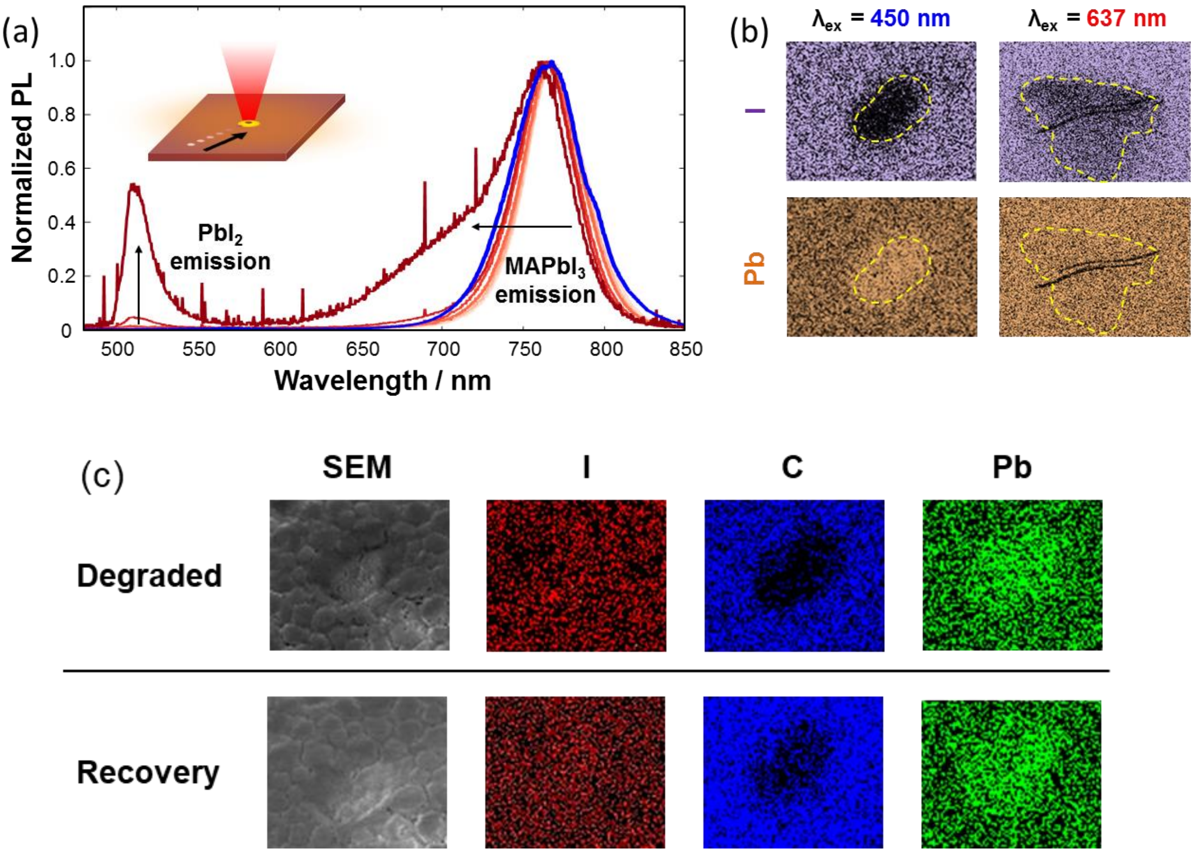

Figure S19 – Degradation as a function of excitation wavelength. (a) PL spectra extracted from different distances away from an irradiated spot of red laser light (637 nm excitation wavelength). Approaching the directly irradiated spot results in a progressive blue-shift of the PL spectra, while the spectrum measured directly in the spot shows a distinct emission peak at 510 nm, which is associated with PbI_2. Prior to reaching the directly irradiated spot, the PL spectrum exhibits a broad shoulder, which is indicative of a distorted lattice. The blue spectrum represents PL measure with excitation at 450 nm similar to the conditions shown in **Figure 1** in the main text, where no emission is observed at 510 nm from which we draw the conclusion that no detectable PbI_2 is present. (b) Energy dispersive X-ray images of iodide and lead acquired from regions of a film exposed to blue and red light. A reduction of I is noted for both excitation wavelength while the Pb signal shows no change for red excitation and an increase for blue excitation, which is indicative of Pb^0 formation. (c) EDX mapping shows the recovery of the sample is potentially due to the ionic defects migration comparing the same spot right after light exposure (30 minutes) and after 2 weeks of resting in the dark, in agreement with our previous study.[3]

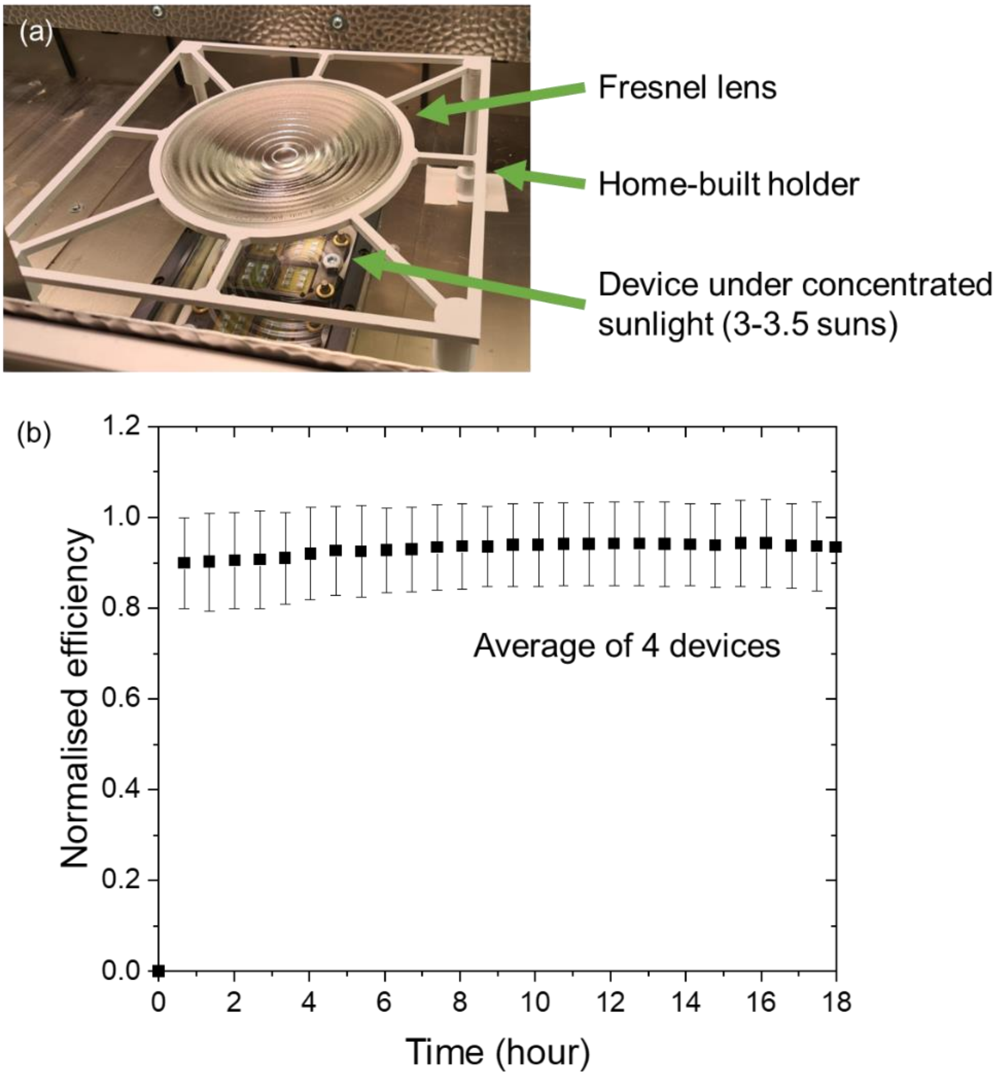

Figure S20 – Concentrated PV for an extended time period. (a) The set-up to concentrate light from a metal halide lamp with 100 W/cm^2 intensity. (b) Normalised efficiency of an average of 4 devices at 3 suns illumination, error bar represents the standard deviation of the 4 devices.

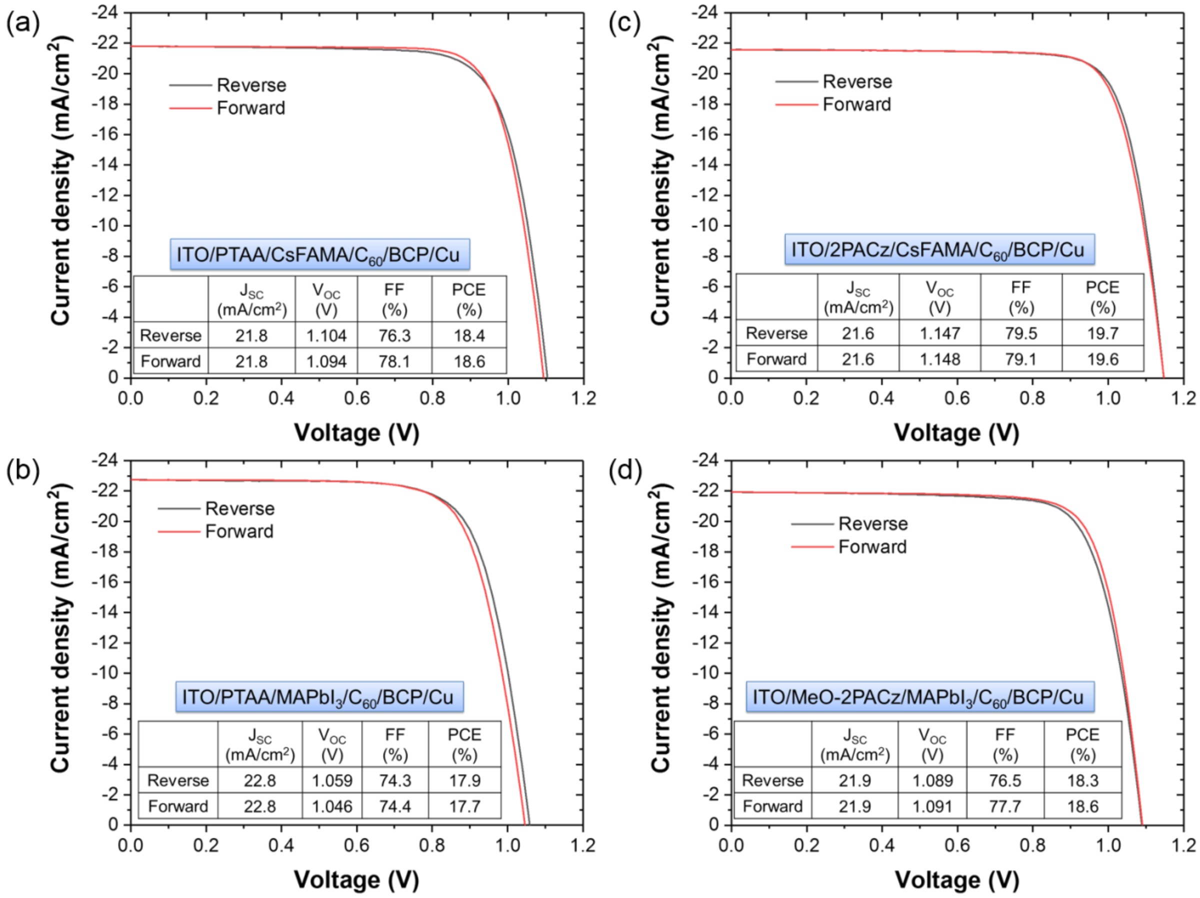

(a)

	J_{SC} (mA/cm^2)	V_{OC} (V)	FF (%)	PCE (%)
Reverse	21.8	1.104	76.3	18.4
Forward	21.8	1.094	78.1	18.6

(b)

	J_{SC} (mA/cm^2)	V_{OC} (V)	FF (%)	PCE (%)
Reverse	22.8	1.059	74.3	17.9
Forward	22.8	1.046	74.4	17.7

(c)

	J_{SC} (mA/cm^2)	V_{OC} (V)	FF (%)	PCE (%)
Reverse	21.6	1.147	79.5	19.7
Forward	21.6	1.148	79.1	19.6

(d)

	J_{SC} (mA/cm^2)	V_{OC} (V)	FF (%)	PCE (%)
Reverse	21.9	1.089	76.5	18.3
Forward	21.9	1.091	77.7	18.6

Figure S21 - J-V of devices used in this study. (a-d) characteristics of different device structures as described in the blue field of each panel.

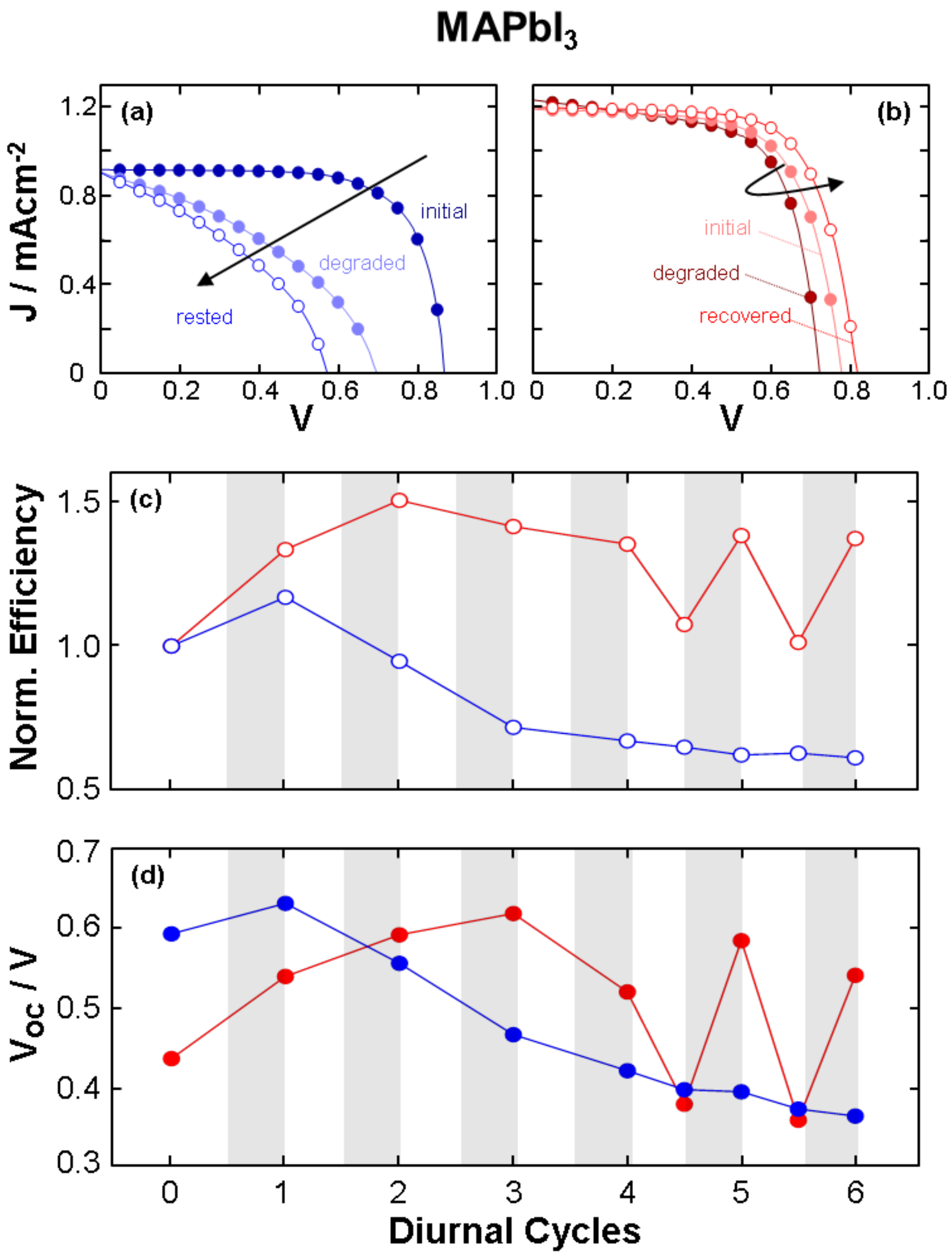

Figure S22 - Day-night cycling aging experiment. 12h Maximum power point (MPP) tracking with red/blue band pass filters in AM1.5 solar simulator light source, and 8h in dark rest of non-encapsulated devices in N_2 environment. (a) and (b) show the current density-voltage (J-V) curves of initial day and before and after dark rest of 7th day with blue or red light aging. The evolution of (c) power conversion efficiency (PCE) and (d) open circuit voltage (V_{OC}) over 7 days of aging (obtained from J-V scans on the first hour of 12 hours MPP tracking).

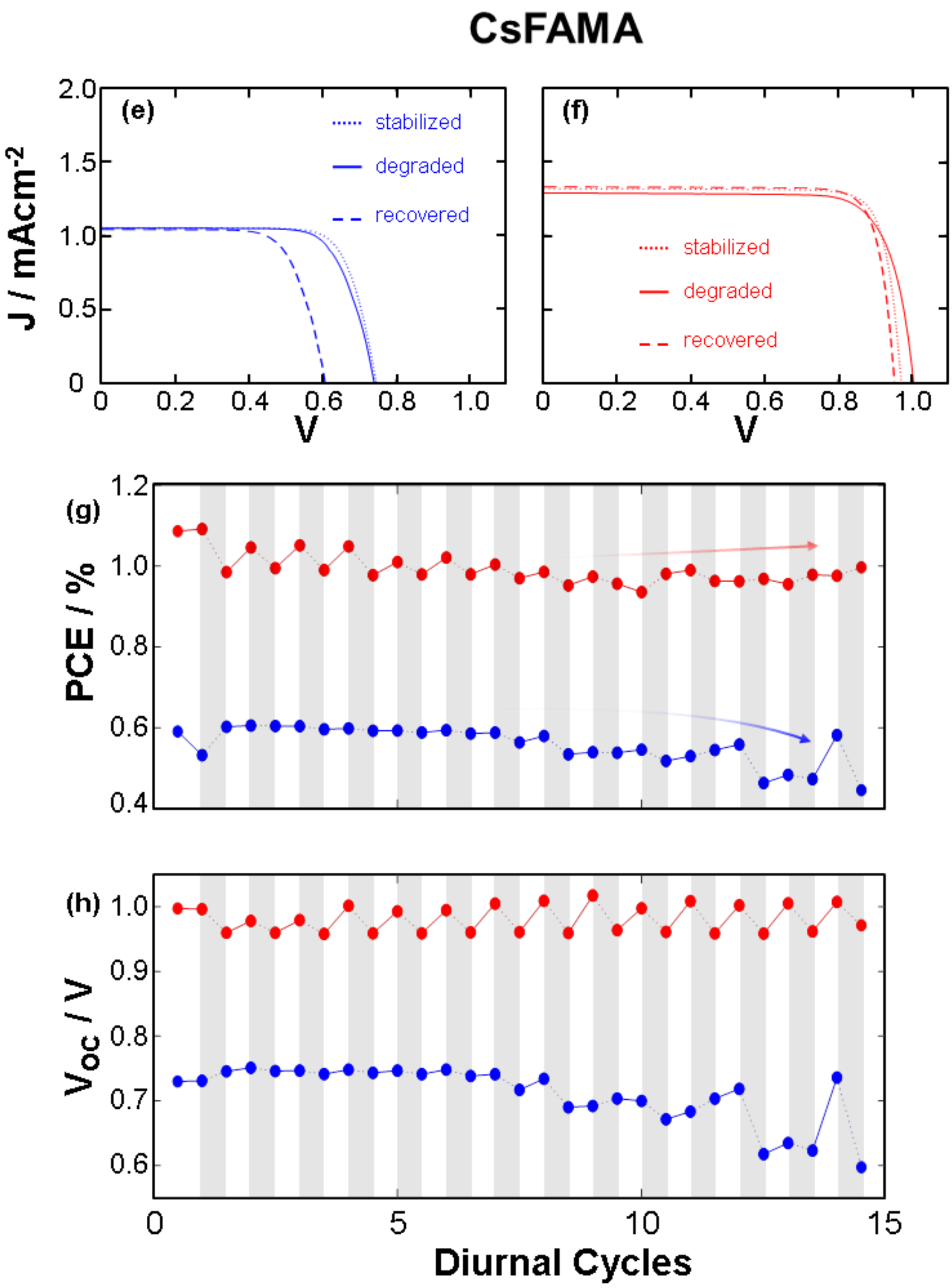

Figure S23 - Aging measurement of triple cation (CsFAMA) devices. (a) and (b) show the current density-voltage (J-V) curves of initial day and before and after dark rest of 14th day with blue or red light aging. The evolution of (g) PCE and (h) V_{OC} over 7 days of aging (obtained from J-V scans on the first hour of 12 hours MPP tracking).

Table 1 – MAPbI$_3$ defect formation energies. Formation energies of iodide and methylammonium Frenkel pairs at various configurations and distances between the corresponding defects (see **Figure S6**) In the table we report both, results obtained by optimizing the geometry of the samples, with and without Frenkel pairs, and from ab initio MD at 300K. In the case of results from MD, we do not report the '∞' case of as here the subtraction of the effect of spurious interactions among periodic images of point charges is tricky. We considered also the case of two Frankel pairs in the 32 stoichiometric units simulations box, denoted as **2 x Iodide Frenkel pairs** and **2 x Methylammonium Frenkel pairs** in the table.

Defect	**Configuration**	**DE [eV]**	
		Opt.	**MD**
Iodide Frenkel pair	1	0.23	0.45
	2	0.43	0.85
	3	0.40	0.8
	4	0.33	0.66
	∞	0.9	-
2 x Iodide Frenkel pairs		0.97	
Methylammonium Frenkel pair	1	0.87	1.05
	2	0.96	1.12
	3	0.82	1.16
	4	0.9	0.94
	∞	1.05	-
2 x Methylammonium Frenkel pairs		1.11	

Table S2 - Fitted parameters for the JMAK kinetics function.

Parameter	**Tetragonal phase**	**Isotropic structure** **(Cubic-like phase)**
t_0 /min	97.5±3.6	97.4±3.6
k /min^{-n}	$4.5 \cdot 10^{-6} \pm 0.2 \cdot 10^{-6}$	$4.5 \cdot 10^{-6} \pm 0.2 \cdot 10^{-6}$
n	2.51±0.02	2.51±0.02

References

1. Chen, S., Wen, X., Huang, S., Huang, F., Cheng, Y., Green, M., and Ho-Baillie, A. (2017). Light illumination induced photoluminescence enhancement and quenching in lead halide perovskite. Sol. Rrl *1*, 1600001.

2. DeQuilettes, D.W., Zhang, W., Burlakov, V.M., Graham, D.J., Leijtens, T., Osherov, A., Snaith, H.J., Ginger, D.S., and Stranks, S.D. (2016). Photo-induced halide redistribution in organic–inorganic perovskite films. Nat. Commun. *7*, 11683.

3. Phung, N., Al-ashouri, A., Meloni, S., Mattoni, A., Albrecht, S., Unger, E.L., Merdasa, A., and Abate, A. (2020). The Role of Grain Boundaries on Ionic Defect Migration in Metal Halide Perovskites. Adv. Energy Mater. *11*, 1903735.

4. Fassl, P., Ternes, S., Lami, V., Zakharko, Y., Heimfarth, D., Hopkinson, P.E., Paulus, F., Taylor, A.D., Zaumseil, J., and Vaynzof, Y. (2019). Effect of Crystal Grain Orientation on the Rate of Ionic Transport in Perovskite Polycrystalline Thin Films. ACS Appl. Mater. Interfaces *11*, 2490–2499.

5. Bai, S., Da, P., Li, C., Wang, Z., Yuan, Z., Fu, F., Kawecki, M., Liu, X., Sakai, N., Wang, J.T.W., et al. (2019). Planar perovskite solar cells with long-term stability using ionic liquid additives. Nature *571*, 245–250.

6. Foley, B.J., Marlowe, D.L., Sun, K., Saidi, W.A., Scudiero, L., Gupta, M.C., and Choi, J.J. (2015). Temperature dependent energy levels of methylammonium lead iodide perovskite. Appl. Phys. Lett. *106*, 243904.

7. Dar, M.I., Jacopin, G., Meloni, S., Mattoni, A., Arora, N., Boziki, A., Zakeeruddin, S.M., Rothlisberger, U., and Grätzel, M. (2016). Origin of unusual bandgap shift and dual emission in organic-inorganic lead halide perovskites. Sci. Adv.

8. Wang, Z., Lin, Q., Wenger, B., Christoforo, M.G., Lin, Y.H., Klug, M.T., Johnston, M.B., Herz, L.M., and Snaith, H.J. (2018). High irradiance performance of metal halide perovskites for concentrator photovoltaics. Nat. Energy *3*, 1013.

9. Heiderhoff, R., Haeger, T., Pourdavoud, N., Hu, T., Al-Khafaji, M., Mayer, A., Chen, Y., Scheer, H.-C., and Riedl, T. (2017). Thermal conductivity of methylammonium lead halide perovskite single crystals and thin films: A comparative study. J. Phys. Chem. C *121*, 28306–28311.

10. De Wolf, S., Holovsky, J., Moon, S.-J., Löper, P., Niesen, B., Ledinsky, M., Haug, F., Yum, J., and Ballif, C. (2014). Organometallic Halide Perovskites: Sharp Optical Absorption Edge and Its Relation to Photovoltaic Performance. J. Phys. Chem. Lett. *5*, 1035–1039.

11. Eames, C., Frost, J.M., Barnes, P.R.F., O’Regan, B.C., Walsh, A., and Islam, M.S. (2015). Ionic transport in hybrid lead iodide perovskite solar cells. Nat. Commun. *6*, 7497.

12. Azpiroz, J.M., Mosconi, E., Bisquert, J., and Angelis, F. De (2015). Defect migration in methylammonium lead iodide and its role in perovskite solar cell operation. Energy Environ. Sci. *8*, 2118–2127.

13. Meloni, S., Moehl, T., Tress, W., Franckevičius, M., Saliba, M., Lee, Y.H., Gao, P., Nazeeruddin, M.K., Zakeeruddin, S.M., Rothlisberger, U., et al. (2016). Ionic polarization-induced current–voltage hysteresis in CH3NH3PbX3 perovskite solar cells. Nat. Commun. *7*, 10334.

14. Mattoni, A., and Meloni, S. (2020). Defect Dynamics in MAPbI 3 Polycrystalline Films: The Trapping Effect of Grain Boundaries. Helv. Chim. Acta, hlca.202000110.

15. Yavari, M., Ebadi, F., Meloni, S., Wang, Z.S., Yang, T.C.J., Sun, S., Schwartz, H., Wang, Z., Niesen, B., Durantini, J., et al. (2019). How far does the defect tolerance of lead-halide perovskites range? The example of Bi impurities introducing efficient recombination centers. J. Mater. Chem. A *7*, 23838–23853.

16. Cohen, A. V, Egger, D.A., Rappe, A.M., and Kronik, L. (2019). Breakdown of the Static Picture of Defect Energetics in Halide Perovskites: The Case of the Br Vacancy in CsPbBr 3. J. Phys. Chem. Lett. *10*, 4490–4498.

17. Fabini, D.H., Laurita, G., Bechtel, J.S., Stoumpos, C.C., Evans, H.A., Kontos, A.G., Raptis, Y.S., Falaras, P., Van der Ven, A., Kanatzidis, M.G., et al. (2016). Dynamic Stereochemical Activity of the Sn 2+ Lone Pair in Perovskite CsSnBr 3. J. Am. Chem. Soc. *138*, 11820–11832.

18. Hoye, R.L.Z., Schulz, P., Schelhas, L.T., Holder, A.M., Stone, K.H., Perkins, J.D., Vigil-Fowler, D., Siol, S., Scanlon, D.O., Zakutayev, A., et al. (2017). Perovskite-Inspired Photovoltaic Materials: Toward Best Practices in Materials Characterization and Calculations. Chem. Mater. *29*, 1964–1988.

19. Steirer, K.X., Schulz, P., Teeter, G., Stevanovic, V., Yang, M., Zhu, K., and Berry, J.J. (2016). Defect Tolerance in Methylammonium Lead Triiodide Perovskite.

20. Ummadisingu, A., and Grätzel, M. (2018). Revealing the detailed path of sequential deposition for metal halide perovskite formation. Sci. Adv. *4*, e1701402.

21. Borchert, J., Boht, H., Fränzel, W., Csuk, R., Scheer, R., and Pistor, P. (2015). Structural investigation of co-evaporated methyl ammonium lead halide perovskite films during growth and thermal decomposition using different PbX 2 (X = I, Cl) precursors. J. Mater. Chem. A *3*, 19842–19849.

22. Nie, W., Tsai, H., Blancon, J.-C.C., Liu, F., Stoumpos, C.C., Traore, B., Kepenekian, M., Durand, O., Katan, C., Tretiak, S., et al. (2018). Critical Role of Interface and Crystallinity on the Performance and Photostability of Perovskite Solar Cell on Nickel Oxide. Adv. Mater. *30*, 1–9.

23. Condeles, J.F., Ando, R.A., and Mulato, M. (2008). Optical and structural properties of PbI2 thin films. J. Mater. Sci. *43*, 525–529.

24. Merdasa, A., Kiligaridis, A., Rehermann, C., Abdi-Jalebi, M., Stöber, J., Louis, B., Gerhard, M., Stranks, S.D., Unger, E.L., and Scheblykin, I.G. (2019). Impact of Excess Lead Iodide on the Recombination Kinetics in Metal Halide Perovskites. ACS Energy Lett. *4*, 1370–1378.

25. Cho, Y., Soufiani, A.M., Yun, J.S., Kim, J., Lee, D.S., Seidel, J., Deng, X., Green, M.A., Huang, S., and Ho-Baillie, A.W.Y. (2018). Mixed 3D–2D Passivation Treatment for Mixed-Cation Lead Mixed-Halide Perovskite Solar Cells for Higher Efficiency and Better Stability. Adv. Energy Mater. *8*, 1–10.

26. Cappel, U.B., Svanström, S., Lanzilotto, V., Johansson, F.O.L., Aitola, K., Philippe, B., Giangrisostomi, E., Ovsyannikov, R., Leitner, T., Föhlisch, A., et al. (2017). Partially reversible photoinduced chemical changes in a mixed-ion perovskite material for solar cells. ACS Appl. Mater. Interfaces *9*, 34970–34978.

27. Hong, Q.M., Xu, R.P., Jin, T.Y., Tang, J.X., and Li, Y.Q. (2019). Unraveling the light-induced degradation mechanism of CH3NH3PbI3 perovskite films. Org. Electron. *67*, 19–25.

28. Turkevych, I., Kazaoui, S., Belich, N.A., Grishko, A.Y., Fateev, S.A., Petrov, A.A., Urano, T., Aramaki, S., Kosar, S., Kondo, M., et al. (2019). Strategic advantages of reactive polyiodide melts for scalable perovskite photovoltaics. Nat. Nanotechnol. *14*, 57–63.

29. Al-Ashouri, A., Magomedov, A., Roß, M., Jošt, M., Talaikis, M., Chistiakova, G., Bertram, T., Márquez, J.A., Köhnen, E., Kasparavičius, E., et al. (2019). Conformal monolayer contacts with lossless interfaces for perovskite single junction and monolithic tandem solar cells. Energy Environ. Sci. *12*, 3356–3369.

30. Tress, W., Yavari, M., Domanski, K., Yadav, P., Niesen, B., Correa Baena, J.P., Hagfeldt, A., and Graetzel, M. (2018). Interpretation and evolution of open-circuit voltage, recombination, ideality factor and subgap defect states during reversible light-soaking and irreversible degradation of perovskite solar cells. Energy Environ. Sci. *11*, 151–165.

31. Saliba, M., Matsui, T., Seo, J.-Y.Y., Domanski, K., Correa-Baena, J.-P.P., Nazeeruddin, M.K., Zakeeruddin, S.M., Tress, W., Abate, A., Hagfeldt, A., et al. (2016). Cesium-containing triple cation perovskite solar cells: Improved stability, reproducibility and high efficiency. Energy Environ. Sci. *9*, 1989–1997.

32. Kim, J.Y., Lee, J.-W., Jung, H.S., Shin, H., and Park, N.-G. (2020). High-Efficiency Perovskite Solar Cells. Chem. Rev. *120*, 7867–7918.

33. Andaji-Garmaroudi, Z., Anaya, M., Pearson, A.J., and Stranks, S.D. (2019). Photobrightening in Lead Halide Perovskites: Observations, Mechanisms, and Future Potential. Adv. Energy Mater. *1903109*, 1–12.

34. Motti, S.G., Meggiolaro, D., Martani, S., Sorrentino, R., Barker, A.J., Angelis, F. De, and Petrozza, A. (2019). Defect Activity in Metal – Halide Perovskites. *1901183*, 1–11.

35. Domanski, K., Roose, B., Matsui, T., Saliba, M., Turren-Cruz, S.-H., Correa-Baena, J.-P., Carmona, C.R., Richardson, G., Foster, J.M., De Angelis, F., et al. (2017). Migration of cations induces reversible performance losses over day/night cycling in perovskite solar cells. Energy Environ. Sci. *10*, 604–613.

36. Khenkin, M. V., Anoop, K.M., Visoly-Fisher, I., Galagan, Y., Di Giacomo, F., Patil, B.R., Sherafatipour, G., Turkovic, V., Rubahn, H.-G.G., Madsen, M., et al. (2018). Reconsidering figures of merit for performance and stability of perovskite photovoltaics. Energy Environ. Sci. *11*, 739–743.

37. Huang, F., Jiang, L., Pascoe, A.R., Yan, Y., Bach, U., Spiccia, L., and Cheng, Y.-B. (2016). Fatigue behavior of planar CH3NH3PbI3 perovskite solar cells revealed by light on/off diurnal cycling. Nano Energy *27*, 509–514.

38. Ceratti, D.R., Rakita, Y., Cremonesi, L., Tenne, R., Kalchenko, V., Elbaum, M., Oron, D., Potenza, M.A.C., Hodes, G., and Cahen, D. (2018). Self-Healing Inside APbBr3 Halide Perovskite Crystals. Adv. Mater. *30*, 1–7.

39. Ibaceta-Jaña, J., Muydinov, R., Rosado, P., Mirhosseini, H., Chugh, M., Nazarenko, O., Dirin, D.N., Heinrich, D., Wagner, M.R., Kühne, T.D., et al. (2020). Vibrational dynamics in lead halide hybrid perovskites investigated by Raman spectroscopy. Phys. Chem. Chem. Phys. *22*, 5604–5614.

40. Steele, J.A., Yuan, H., Tan, C.Y.X., Keshavarz, M., Steuwe, C., Roeffaers, M.B.J., and Hofkens, J. (2017). Direct Laser Writing of δ- to α-Phase Transformation in Formamidinium Lead Iodide. ACS Nano *11*, 8072–8083.